Graduate Theses and Dissertations   Graduate School

January 2012

Numerical Simulation of Sliding Friction and Wet Traction Force on a Smooth Tire Sliding on a Random Rough Pavement

Janaka Vishwanath Kosgolla
University of South Florida, jkosgoll@mail.usf.edu

Follow this and additional works at: http://scholarcommons.usf.edu/etd

Part of the Civil Engineering Commons

Numerical Simulation of Sliding Friction and Wet Traction

Force on a Smooth Tire Sliding on a Random Rough Pavement

by

Janaka V. Kosgolla

A dissertation submitted in partial fulfillment
of the requirements for the degree of
Doctor of Philosophy
Department of Civil and Environmental Engineering
College of Engineering
University of South Florida

Major Professor: Manjriker Gunaratne, Ph.D.
Daniel Simkins, Ph.D.
Daniel Hess, Ph.D.
Andres Tejada, Ph.D.
Razvan Teodorescu, Ph.D.
Qing Lu, Ph.D.

Date of Approval:
November 28, 2012

Copyright © 2012, Janaka V. Kosgolla

DEDICATION

To my wife Dulmin Jayawardana and my son Asel Nethan Kosgolla and my parents.

ACKNOWLEDGMENTS

TABLE OF CONTENTS

LIST OF TABLES

LIST OF FIGURES

ABSTRACT

Availability of analytical and numerical tools that can provide reliable and accurate estimates of wet frictional resistance in different pavements would preclude the need for time consuming field tests. Therefore, many research efforts have been made to develop such tire-pavement friction predictive tools that are invaluable for friction management programs. However, due to the complexity of the problem, most existing tools have been developed based on several simplifying assumptions and without field verification of their predictions. The current study is focused on the evaluation of two specific prediction methods that can be used to predict friction on a smooth tire sliding on a rough moist pavement by comparing the corresponding predictions with the results of field experiments. A 3-dimensional finite element model (FEM) formulated in ANSYS software and an analytical method based on computing hysteresis friction from viscous energy dissipation are the two methods considered in this study. Both prediction tools are capable of considering rough pavement surface texture while the FEM method can even incorporate the specific tire geometric and material properties. Friction predictions of the two methods based on the macrotexture data collected at a selected test surface provide reasonably accurate results when compared to the corresponding field evaluation. The main finding of the investigation is the availability of relatively easily executed analytical methodologies that are comparable in accuracy to more rigorous finite element tools.

The second stage of the research was focused on wet weather friction of a tire sliding on a randomly rough pavement. A numerical model was developed to predict the

drag force of a sliding tire on a wet rough pavement. The model consists of three sub-models; the fluid model based on the Reynolds equation, tire model developed with two sets of springs and a rigid pavement model. As a contribution to the state-of-the-art the author modeled the pavement by including randomly rough properties which represent real pavements. The results of the parametric study based on the model predictions are agreeable with physical principles and intuition. However, this model is only capable of simulating laminar water flow between the tire and the pavement whereas in reality turbulent flow can occur very often on a randomly rough pavement.

CHAPTER 1

PRELIMINARY STUDY OF DRY FRICTION

1.1 Introduction

The study and evaluation of tire pavement friction have drawn renewed interest during the last few decades because of the need for effective friction rehabilitation on highways and runways mandated by stringent friction management programs. However, accurate prediction of friction on wet pavements that lead to vehicle skidding is still a partially solved problem that involves a multitude of many factors affecting tire pavement friction such as tire inflation pressure, sliding or rolling speed, vertical load, geometry, cross-sectional properties, material properties and pavement surface texture characteristics. Tire friction models can be divided into two categories as static friction models and dynamic friction models. Static friction models are appropriate for steady-state operating conditions and the most widely used one being the Pacejka's magic formula [2]. On the other hand, the dynamic tire models become more accurate when a tire is under braking or acceleration. Although accurate dynamic models have been developed recently, those models are not any more capable of modeling very important tire pavement friction parameters such as geometric and material properties of tire and texture properties of pavement than prediction tools that had existed. The Dhal model, bristle model and Lugre model are some examples of dynamic friction models [1, 2]. The motivation behind this work is the need for accurate and reliable prediction tools

of tire pavement friction particularly under wet conditions because more accidents are caused during wet weather conditions. Therefore, the work reported in this paper is concerned with the development of a numerical model and an analytical model for predicting the sliding friction of a smooth tire on a rough moist pavement surface and comparison of the corresponding predictions with the results of field experiments. The proposed numerical model (based on finite element software ANSYS) has the capability of simulating pavement macrotexture characteristics, tire geometric and material properties, tire pressure, vertical loading and sliding of the tire. It can be used to evaluate the hysteretic friction under steady state sliding conditions. On the other hand, the proposed analytical tire model directly predicts the hysteretic friction of a sliding tire on a random rough pavement surface based on fundamental concepts of hysteretic friction.

1.2 Components of pavement friction

The two major independent mechanisms which contribute to sliding friction of rubber are adhesion and hysteresis. Adhesion friction depends on the intermolecular-kinetic, thermally activated stick-slip mechanism which takes place essentially at the sliding interface [3]. Elastomer structures like rubber are composed of flexible molecular chains. During relative sliding between an elastomer and a rigid surface the polymer chains in the elastomer slide relative to each other. This causes forming and breaking of local bonds leading to an energy loss. Thus, it is the pavement microtexture that contributes mostly to adhesion. On the other hand, hysteretic friction depends on the viscoelastic characteristics of rubber and depends directly on the energy dissipation inside the material due to the frequency of indentation by the pavement macrotexture. The existence of varying roughness levels on a given pavement yields a considerable range of

indentation frequencies during one sliding maneuver. According to Moore [4], adhesion friction peaks occur at lower sliding velocities while hysteretic friction peaks occur at higher sliding velocities. Since adhesion plays an insignificant role in producing friction on moist surfaces, this component of friction is not considered in this study.

1.2.1 Pavement friction characteristics

1.2.1.1 Effect of pavement texture

Although the exact mechanism of tire-pavement friction interaction is not fully understood, it is generally agreed that the frictional force is composed mainly of adhesion and hysteresis components. As depicted in Figure 1.1 adhesion is generated in overcoming the work required for successive formation and breaking of bonds between the tire molecules and the pavement micro-texture as the tire traverses the pavement surface while being tightly pressed against it by the vehicle weight. Pavement micro-texture defines the exact surface of the aggregate asperities with its magnitude ranging from 1 to 500μm (0.5mm) [2]. Therefore, it is reasonable to assume that the adhesion component of pavement friction is only significant on dry pavement surfaces at low vehicle slip speeds when there is ample opportunity for tire-pavement bonding. On the other hand, hysteresis is generated when the tire overcomes the work required to drape around pavement macro-texture profile defined by the arrangement and orientation of aggregate particles on the pavement surface. Macro-texture is generally considered to have a magnitude in the range of 0.5 - 50 mm [2]. On the other hand pavement profile deviations exceeding 50 mm are due to the pavement unevenness or roughness [2] and are termed mega-texture in pavement friction studies. Thus, the hysteresis component of

friction increases with speed and provides the bulk of skid resistance at relatively higher speeds even on wet pavements when the macro-texture is exposed above the water film.
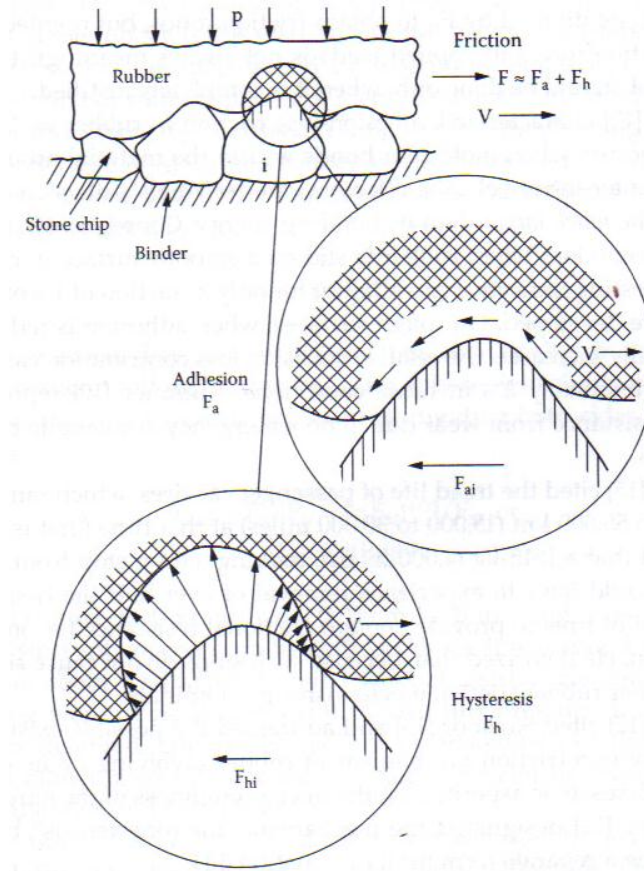
Figure 1.1: Basic mechanisms of friction

Shearing of tire rubber leading to tire wear is another factor that contributes to the frictional force, although at a negligible magnitude when compared to the adhesion and hysteresis components. Thus, one can express the frictional coefficient which is the ratio of the frictional force to the normal load at the footprint as;

$$f = f_{ad} + f_{hy} \qquad (1.1)$$

1.2.1.2 Effect of speed and temperature

Rubber is a viscoelastic material where damping properties depend strongly on the sliding speed and the temperature. Kummer [12] investigated the effect of speed and

temperature and concluded that when speed is low (0 to 10 mph), the adhesion force component shows significant speed dependence. However, the hysteresis force component shows a little speed dependence. When speed is very high (i.e. >50 mph), the adhesion force component coefficient remains relatively stable and the hysteresis force component begins to increase noticeably, especially after 50 mph. Figure 1.2 shows the typical dependences of adhesion and hysteresis force components on sliding speed. As temperature increases, the adhesion force component may increase or decrease. However, the hysteresis force component always decreases as temperature increases.
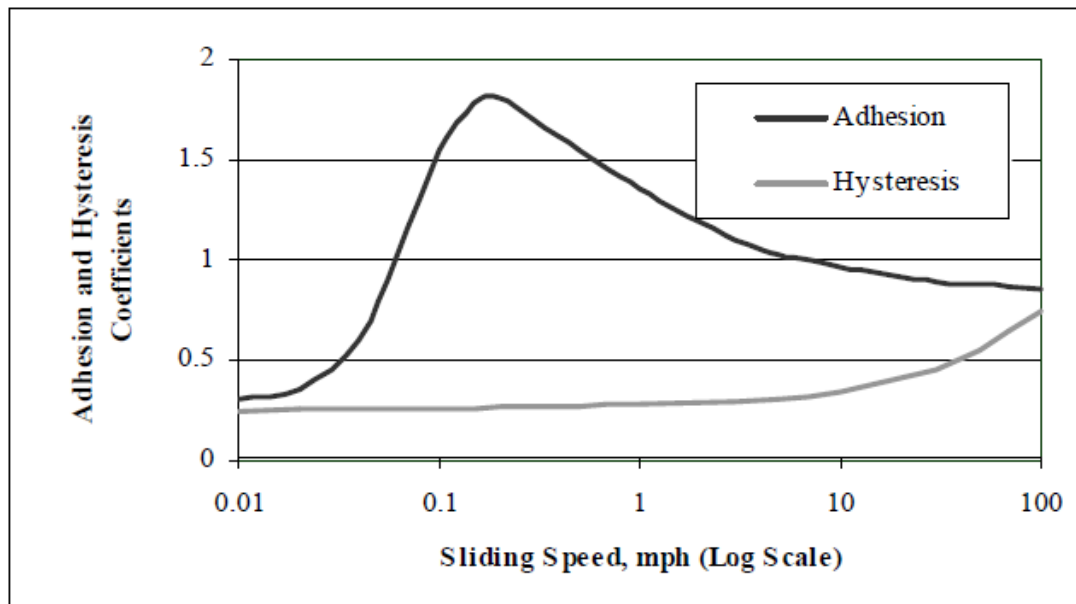
Figure 1.2: Dependences of adhesion and hysteresis on sliding speed

1.3 Hydroplaning phenomenon

Basically, there are two types of hydroplaning: (1) viscous hydroplaning and (2) dynamic hydroplaning. Both viscous and dynamic hydroplaning can degrade both the braking and directional controllability of an aircraft.

1.3.1 Viscous hydroplaning

This can occur on wet runways and is a technical term used to describe the normal slipperiness or lubricating action of water. Viscous hydroplaning occurs when a tire is unable to puncture the thin residual film of water left on a paved surface. This water lubricates the surface and reduces its friction. This type of lubrication can be reduced by making the pavement surface rough. When the water film thickness is relatively high and covers the average level of macro-texture, the contributions from both adhesion and hysteresis diminish drastically with increasing speeds in particular.

1.3.2 Dynamic hydroplaning

This is the phenomenon that is normally referred to as aquaplaning. It can occur when an aircraft lands fast enough on a sufficiently wet runway. When the aircraft's speed and water depth are sufficient, inertial effects prevent the water from escaping from the tire footprint area, and the tire is held off the pavement by the hydrodynamic uplift force. Dynamic hydroplaning is also a function of tire pressure. Studies indicate that the minimum speed (in knots) for dynamic hydroplaning to occur is approximately $9\sqrt{p}$, where p is the tire pressure in psi [3]. Figures 1.3(a) and 1.3(b) illustrate the difference between the typical wet rolling condition of a tire and the onset of dynamic hydroplaning. The condition shown in Figure 1.3(a) is experienced by vehicle or aircraft tires under safe operational modes in wet weather.
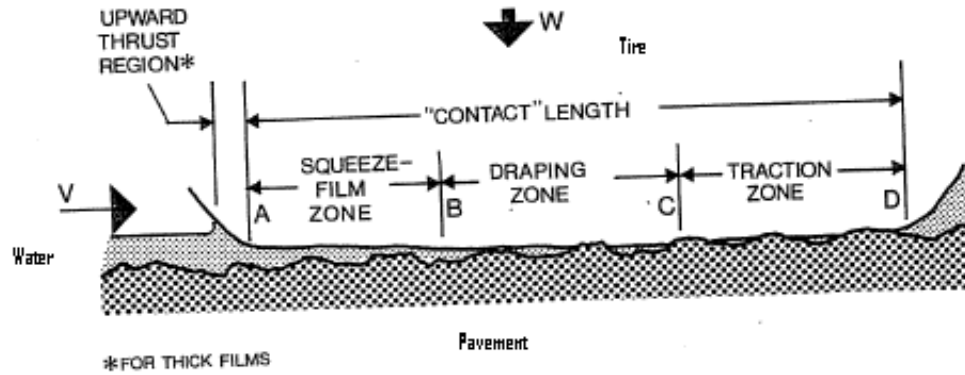
Figure 1.3 (a): Interaction between tire and wetted pavement
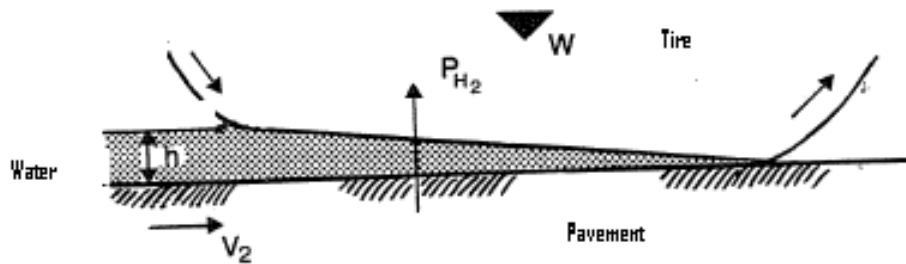
Figure 1.3 (b): Onset of dynamic hydroplaning under excessive water

1.3.2.1 Effect of water film thickness (water depth)

Many researchers [9, 10, 11] have observed that water depth is of little or no consequence below about 35 mph perhaps because the duration of the load pulse induced by the tire at a particular pavement location. The squeezing effect can be expressed approximately by the ratio of length of foot print/speed, is adequate for water to be drained (or squeezed) out from the footprint area under common unworn pavement macro-texture and unworn tire tread depth. However, there is a substantial reduction in the level of friction due to wetting at any speed. Moreover, as the vehicle speed increases above 35 mph, drainage of water from the tire footprint is retarded within the duration of the tire stress pulse, giving rise to dynamic hydroplaning. The onset of dynamic

7

hydroplaning is clearly seen here for different water thicknesses. Hydroplaning occurrence depends on two necessary conditions: (1) appropriate water film thickness for a certain level of rainfall intensity, and (2) actual driving speeds that match or exceed the hydroplaning speed corresponding to a given water film thickness.

1.4 Problems with pavement friction characteristics

Aircraft accidents/incidents reports have identified that almost one in three landing approaches is not stabilized although not all the unstabilized approaches result in a runway overrun or excursion. Most of these occur under runway conditions that are reported as "wet" and in most of the cases, the landing before the accident had been normal [14].

There is no straightforward definition of a "wet" runway in Federal Aviation Administration (FAA) rules. However the criteria have several "grey areas" and the only information that a pilot acquires is based on the assumption that the water depth is less than 2.5 mm when the runway is reported wet. The air traffic controllers rarely report "contaminated" or "slippery" conditions. The wet runway condition becomes more critical in heavy rain and in cross wind. Even for grooved and sloped runways, the water depth can be more than 15 mm during the period of heavy rain. The depth of water or slush, exceeding approximately 2.5 mm over a considerable proportion of the length of the runway can have an adverse effect on the landing performance [15]. Under such conditions hydroplaning is likely to occur with the associated problems of negligible wheel-braking and loss of directional control. Moreover, once hydroplaning is established it may, in certain circumstances, be maintained in much lower depths of water or slush.

In a Civil Aviation Authority report [16] for risks and factors associated with operations on runways affected by snow, slush or water indicates classification of the presence of water on a runway depending on the condition. A number of safety recommendations were made in that incident report including the one that the CAA (Civil Aviation Authority) must encourage research that could lead to the production of equipment that can accurately measure the braking action on runways under all conditions of surface contamination. In summary it is recommended that the approximation of 2.5 mm water depth which is used to identify if a runway is contaminated, is not well defined and not well studied in any previous work.

1.5 Pavement friction testing

It is the common practice adopted in the industry to estimate coefficient of friction (μ) in wet pavements by measuring the friction and normal forces at the tire pavement interface. Dependence of μ on the speed of travel and the slip ratio is well known and therefore most of the devices operate under standard speed and slip conditions.

1.5.1 Spot measuring devices

Spot measuring devices measure dynamic coefficient of friction at selected locations on the pavement. The British Pendulum Tester (BPT) and the Dynamic Friction Tester (DFT) are examples of such devices.

1.5.1.1 British Pendulum Tester (BPT)

BPT measures the energy loss when a rubber slider edge is propelled over a test surface. This device has been used for pavement friction measurement for several decades. The test result is reported as the British Pendulum Number (BPN). BPT is fitted

with a scale that measures the recovered height in terms of the BPN over a range of 0 to 140. BPN is measured directly using a drag pointer. The greater the friction between the rubber slider and the test surface, the greater the BPN. BPN mainly depends on the microtexture because the slip speed is very low.

1.5.1.2 Dynamic Friction Tester (DFT)

The dynamic friction tester is a portable device for measuring friction. This device consists of a horizontal spinning disk fitted with three spring-mounted rubber sliders. During testing, the disk is lowered so that the three sliders are in contact with the test surface under a constant force normal to the test surface. The disk is driven by a motor and rotates at a tangential speed varying from 0 to 50 mph (80 km/h) which is determined from the rotary speed of the disk. Water is delivered to the test surface by a water supply unit. The horizontal force required to overcome friction is measured by a transducer. The test result is reported as the coefficient of friction and is plotted against the speed (Figure 1.4).
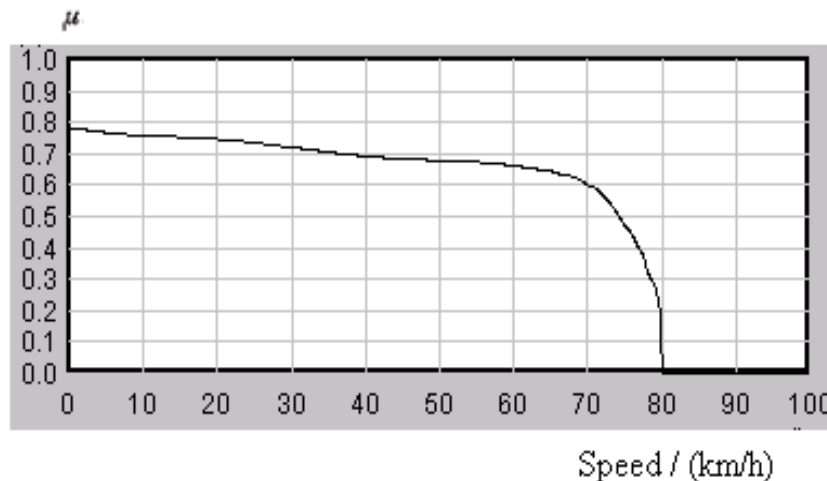
Figure 1.4: Friction data provided by a typical DFT test

1.6 Continuous Friction Measuring Equipment (CFME)

CFME devices provide a real time and continuous estimates of μ on a selected straight segment of a pavement. There is a wide range of operating mechanisms employed in numerous CFMEs and generally different types of wheels are used on them.

1.6.1 Locked Wheel Skid Tester (LWST)

The above device consists of a trailer towed by a vehicle with the test wheels fitted in the trailer. It measures the steady-state friction force on a locked wheel as it slides over a wetted pavement surface under a constant vertical load and at a constant speed. The test tire is either a standard ribbed tire or a standard smooth tire. The apparatus includes force and speed transducers, control system, record system, and pavement wetting system. The test tire inflation pressure is set at 24 psi (165 kPa). In the course of testing, the vehicle reaches the desired speed. Then, water is delivered to the pavement and the test wheel brake is locked 0.5 seconds after beginning of the water delivery. The watering system should provide a water film of 0.02 in. (0.5 mm) at the standard speed of 40 mph (64 km/h).

When the test wheel is locked, this device produces a 100% slip condition under which the relative velocity between the surface of the tire and the pavement surface, i.e., the slip speed, is equal to the vehicle speed. The wheel should remain locked for approximately 1.0 second and the data is measured and averaged. The test results are reported as skid numbers, which are the product of 100 and the coefficient of friction. At very low speeds it is hard to adjust the water delivery.

1.6.2 Runway Friction Tester (RFT)

The Runway Friction Tester (RFT) is an example of a non-locked-wheel fixed slip device. RFT has a separate test wheel to measure friction and a typical RFT operates at a constant slip ranging between 0.1 and 0.15. However, the test mechanism is attached at the rear of a truck behind the tear-wheel axle. Friction measurements obtained by this device tend to be higher than those from a LWST because it operates at a slip at which the frictional force is closer to its maximum with respect to slip. RFT data is reported at each foot of the tested length.

1.6.2.1 Problems with friction measuring devices

Different types of devices employed to measure friction in different parts of the world and disparate reporting formats and scales lead to confusion especially in situations such as runway operations. Additionally, measuring of friction using CFMEs in contaminated pavements are erroneous because contaminant drag on the equipment's measuring wheel, amongst other factors, will cause the reading obtained in these conditions to be unreliable.

1.7 Pavement friction modeling

Although the efforts have been made to model pavement friction through centuries, capturing important frictional behavior in both static and sliding conditions using a single model has been problematic. In this chapter, various friction models will be discussed while categorizing them in to Classical, Steady state and Dynamic models.

1.7.1 Classical friction models

The classical friction models use different combinations of Coulomb friction, viscous friction and Stribeck effect and they are described by static maps between velocity and friction force [17]. Initial development of these friction models for control systems had considerable attention paid to modeling of zero velocity and velocity reversal nature of friction while modeling sliding friction. Since zero velocity and velocity reversal are not experienced in tire pavement friction measuring devices, the above condition is beyond the scope of this research. Moreover, static models do not explain observations such as the hysteresis behavior of friction with varying velocity, variation of the limiting static frictional force and small displacements at the interface during friction.

1.7.2 Steady state and dynamic friction models

Models that can incorporate trivial dynamic effects must be used for more precise description of friction under certain conditions. The first motivation for development of dynamic friction models was precision and friction compensation requirements in controls. The Dahl model [8] is a very early model formulated to serve this purpose. Later on new empirical and analytical models have been developed by various researchers.

1.7.2.1 Schallamach theory

For a rubber tire sliding on a rigid surface, the friction between the tire and the rigid surface are not constant and are strongly dependent on the temperature and the velocity. Schallamach [18, 19] investigated the dynamic friction behavior of the rubber materials. He considered the friction as a molecular-kinetic process due to the thermal

motion of the molecular chains in the rubber surface and presented an exponential relationship among velocity, temperature, and friction.

This model indicates that in the sliding process, the dragging force must be large enough to overcome the activation energy which is the energy barrier created due to molecular bonds. When some molecular bonds are broken, new ones will be formed. As rubber deforms, some areas are compressed and some other areas are stretched. All these phenomena such as molecular bond breaking, bond forming, and body deformation and relaxation consume energy. Therefore, forces arise at the contacting surfaces. The resultant forces depend on the velocity, temperature; and material properties. This model does not consider the effect of adhesional friction.

1.7.2.2 The Penn State models

Researchers in Pennsylvania State University (PSU) have made efforts to investigate the tire-pavement friction phenomenon and develop friction models in the past decades. Based on the fundamentals of rubber friction, Kummer [12] proposed a model to evaluate pavement friction directly using the adhesion and hysteresis components. Other researchers at PSU developed some friction models based on the pavement surface textures because adhesion and hysteresis components are still not fully understood. Leu and Henry [20] presented a model to relate the friction to slip speed by an exponential function.

1.7.2.3 Finite Element (FE) models

Recently, finite element modeling capabilities have been advanced in order to model complex frictional characteristics [9, 10, 11]. Cho [10] proposed a method to estimate the frictional energy loss based on a numerical-analytical approach. Fwa and

Ong [9, 11] developed an analytical computer model to simulate the phenomenon of hydroplaning. They adopted a theoretical approach and proposed an analytical computer model to simulate hydroplaning as well as the reduction of wet-pavement skid resistance as the sliding wheel speed increases. Their theoretical formulation and development of a three-dimensional finite-element model based on solid mechanics and fluid dynamics is presented and their model was analyzed and verified against the well-known experimentally derived NASA hydroplaning-speed Equation This brought researchers a step closer to understand the friction phenomenon and make it possible to characterize tire-pavement friction interaction in terms of the energy dissipation.

1.7.3 Problems with available friction models

While many models have been developed to evaluate pavement friction [9,10,11,21], it is widely accepted that the true pavement friction is hard to determine due to many complex factors involved in the tire-pavement interaction process. Previous researches had not been able to verify their FE models for friction since those models are not capable of handling micro texture level friction. Also those friction models are incapable of handling the viscous hydroplaning condition. The dynamic hydroplaning models developed before such as Fwa and Ong [9, 11], are also incapable of predicting hydroplaning speeds based on pavement texture and drainage characteristics.

1.8 Research methodology

The main objective of this study is to simulate dry, viscous and wet friction and to compare the results with field experiments. FE model developed will be improved such that the model is capable of simulating dry friction including micro friction. Modeling of friction under viscous hydroplaning condition is the second stage of the FE modeling.

1.8.1 Mechanical formulation of equilibrium equations

The generalized Newton's law of motion which is conservation of linear and angular momentum to a deformable solid is applied under steady state conditions. The Cauchy equation of equilibrium for a solid is expressed as;

$$\nabla \cdot \boldsymbol{\sigma} + \rho \mathbf{b} = \rho \mathbf{a} \tag{1.2}$$

where, $\boldsymbol{\sigma}$ denotes the Cauchy stress, $\mathbf{b}$ is the body force, $\mathbf{a}$ is the acceleration of a solid body with mass density ρ.

To compute the friction coefficient, a constant velocity boundary condition was applied. Furthermore, the body forces $\mathbf{b}$ are assumed to be zero because a vertical pressure that includes all external loads and the weight of the rubber block was also applied. Since rubber is a viscoelastic material, in general, the stress is a function of the displacement, $\mathbf{u}$, and velocity, $\dot{\mathbf{u}}$ leading to the reduced equilibrium equation;

$$\nabla \cdot \sigma(u, \dot{u}) = 0 \tag{1.3}$$

The finite element formulation is performed by using a total Lagrangian formulation solving the weak form of the equilibrium equation (Equation 1.4) including the contact model. For each of the two scales, the weak form of the equilibrium equation with respect to the initial configuration follows;

$$\int_{B_i} (\boldsymbol{S} : \delta \boldsymbol{E} - \rho_0 \, \overline{\boldsymbol{b}} . \, \delta \boldsymbol{u}) dV - \int_{\Gamma_{ci}} \overline{t} \, \delta \boldsymbol{u} d\Gamma + \int_{\Gamma_{ci}} p_N \, \delta g_N d\Gamma = 0 \tag{1.4}$$

Here $\boldsymbol{S}$ is the second Piola-Kirchhoff stress, $\boldsymbol{E}$ denotes the Green-Lagrange strains, $\rho_0 \overline{\boldsymbol{b}}$ the body forces, $\overline{t}$ the applied surface tractions, $\delta \boldsymbol{u}$ are the test functions and p_N is the normal contact pressure. While the block discretized by finite elements is pulled over the surface the resulting forces on the upper side of the block can be computed. The

sum of the vertical forces naturally matches the applied pressure multiplied by the top area of representative contact element;

$$\sum F_V = \sigma_V A^{top} = \langle p_N \rangle A^{top} \tag{1.5}$$

where, $\langle p_N \rangle = \frac{1}{\Gamma_{ci}} \int_{\Gamma_{ci}} p_N \, d\Gamma$. These forces are equivalent to the normal forces at the contact area and thus represent the total contact force of the representative contact element.

1.8.1.1 Energy dissipation during sliding

The hysteresis loop can be drawn using the stress-strain diagram as in Figure 1.6. The area under the hysteresis loop is calculated in order to estimate the hysteretic energy loss by assuming the entire energy loss contributes to generate friction without considering thermal or any other losses. Therefore, the hysteresis frictional work equals the dissipated energy in the rubber which can be computed by the area under the hysteresis loop as expressed in the Equation 1.6.

$$\Delta E = \int^T \int^V \sigma \dot{\varepsilon} \, dV \, dt \tag{1.6}$$

where, V is the volume of the body and T is the time concerned.
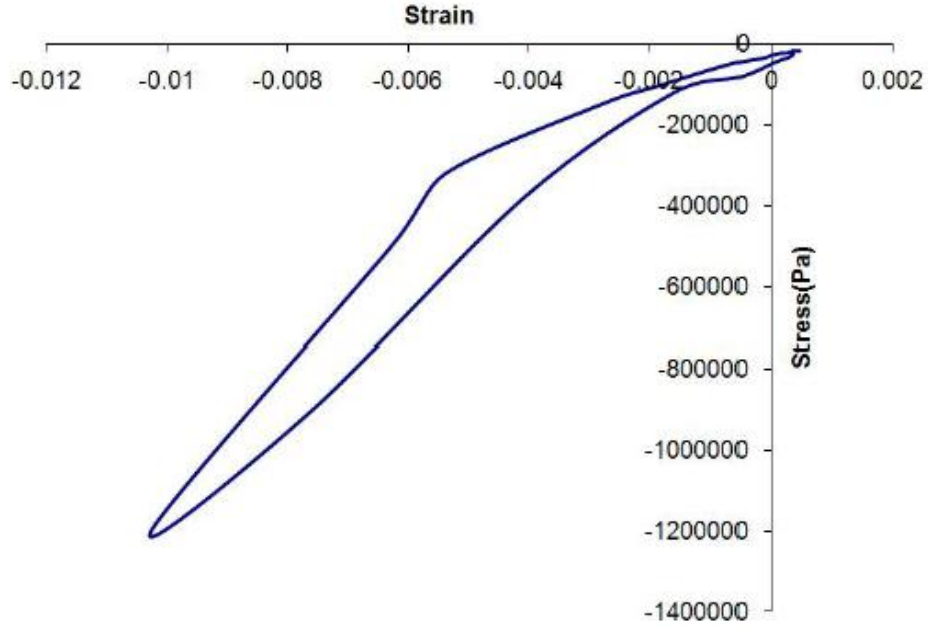
Figure 1.5: A hysteresis loop plotted to a selected node in the rubber block

A program is developed to estimate the total hysteresis energy loss for a sliding distance corresponding to one hysteresis loop. The process has been repeated for each element in the rubber block and individual energies are summed-up to estimate the total energy loss. The total horizontal drag force $\langle F_H \rangle$ is calculated, using the sliding distance l_s and the total energy dissipation (ΔE_{tot});

$$\langle F_H \rangle = \frac{\Delta E_{tot}}{l_s} \tag{1.7}$$

The resulting friction coefficient yields;

$$\langle \mu \rangle_i = \frac{\langle \sum F_H \rangle}{\sum F_V} \tag{1.8}$$

which depends on the sliding velocity v and the averaged contact pressure $\langle p_N \rangle$. Now an analytical friction function $\langle \mu \rangle_{(\langle p_N \rangle, v)}$ is fitted with the simulation results.

1.8.1.2 Implementation of ANSYS finite element model

The finite element program was developed using the ANSYS 12.0 software in two stages. The initial stage models dry sliding friction and the second stage simulates viscous hydroplaning.

1.8.1.2.1 Material properties

Styrene Butadiene Rubber (SBR) is the major material used to manufacture tires. SBR behaves as a hyperelastic material as well as a viscoelastic material. Hyperelasticity refers to materials which can experience a large elastic strain that is recoverable and viscoelasticity refers to the viscous properties. Therefore, a combined hyperelastic and viscoelastic model is used in this simulation.

1.8.1.2.2 Hyperelastic material model

Hyperelasticity has to be considered in the stress-strain behavior of nonlinear elastic material undergoing large deformations. The stress-strain characteristics for hyperelastic materials is derived from the principle of virtual work using the strain energy potential function W, which can be expressed as the invariants of either left or right Cauchy deformation tensors. A material is considered as hyperelastic if one can derive a strain energy density function W, which is a scalar function of the strain or deformation tensors that can be expressed by;

$$S_{ij} = \frac{\partial W}{\partial E_{ij}} \equiv 2\frac{\partial W}{\partial C_{ij}} \tag{1.9}$$

where, S_{ij} are components of the second Piola-Kirchhoff stress tensor, W is strain energy function per unit undeformed volume, E_{ij} are components of the Lagrangian strain tensor, and C_{ij} are components of the right Cauchy-Green deformation tensor. The Lagrangian

strain can be expressed as follows;

$$E_{ij} = \frac{1}{2}(C_{ij} - \delta_{ij}) \tag{1.10}$$

where, δ_{ij} is Kronecker delta. The deformation tensor C_{ij} is comprised of the products of

$C_{ij} = F_{ki}F_{kj}$ where; F_{ij} = components of the deformation gradient tensor, The Kirchhoff

stress can be defined as, $\tau_{ij} = F_{ik}S_{ki}F_{jl}$

The Eigen values of C_{ij} exist only if $det\left[C_{ij} - \lambda_p^2\delta_{ij}\right] = 0$ therefore,

$$\lambda_p^6 - I_1\lambda_p^4 + I_1\lambda_p^2 - I_3 = 0 \tag{1.11}$$

where; I_1, I_2, and $I_{2.5}$ = invariants of C_{ij}

$$I_1 = \lambda_1^2 + \lambda_2^2 + \lambda_3^2 \tag{1.12}$$

$$I_2 = \lambda_1^2\lambda_2^2 + \lambda_2^2\lambda_3^2 + \lambda_3^2\lambda_1^2 \tag{1.13}$$

$$I_2 = \lambda_1^2\lambda_2^2\lambda_3^2 = J^2 \tag{1.14}$$

and $J = det\left[F_{ij}\right]$.

Under the assumption of isotropic material response, the strain energy function

can be expressed in terms of strain invariants.by considering volume preservation;

$$\bar{F}_{ij} = J^{-\frac{1}{3}}F_{ij} \tag{1.15}$$

and therefore, $\bar{J} = det\left[\bar{F}_{ij}\right] = 1$. Then the strain energy potential can then be defined as;

$$W = W(I_1, I_2, J) = W(\bar{\lambda}_1, \bar{\lambda}_2, \bar{\lambda}_3, J) \tag{1.16}$$

The two parameter Mooney-Rivlin material model is used as the hyperelastic

material model. In the Mooney-Rivlin model the strain energy density function is a linear

combination of two invariants of the left Cauchy-Green deformation tensor. Hence it can

be written as;

$$W = C_1(I_1 - 3) + C_2(I_2 - 3) \tag{1.17}$$

I₁ and *I₂* are first and second invariants of the deviatoric component of the left

Cauchy-Green deformation tensor. *C₁* and *C₂* are empirically determined material

constants. Experiments performed by researchers [3], [4], [5] have been used to estimate the constants in the current study.

1.8.1.2.3 Viscoelastic material model

Viscoelastic materials demonstrate the combined characteristics of an elastic solid and a viscous liquid. Conventional theory of viscoelasticity can basically be divided into two categories: linear viscoelasticity and non-linear viscoelasticity. Since, nonlinear viscoelastic material models describe the rubber properties better than linear viscoelastic material models, a nonlinear viscoelastic material model is used in this study. For a viscoelastic material the relaxation modulus of the material during stress relaxation is given by;

$$E(t) = E_e + \sum_{n-1}^{m} E_n exp\left(-\frac{t}{\rho_n}\right)$$ (1.18)

where, E_e = equilibrium modulus, E_n = relaxation strength, ρ_n = a positive constant and t = lapse of time after the load releases. There is another way of representing the strain energy density function in the form of Prony series as expressed below;

$$W(t) =_0^t W x R(t); R(t) = 1 - \sum_{n-1}^{m} \delta_n \left(1 - exp\left(-\frac{t}{\lambda_n}\right)\right)$$ (1.19)

where, $W(t)$ is strain density function, t is time and δ_n, λ_n are Prony constants ([3], [4] ,[5]). Experiments performed by [3], [4], [5] have been used to estimate the constants in this study. $R(t)$ is the relaxation function. Prony series material constants are defined based on numerical experiments and empirical relationships in [4] and [5].

1.8.1.2.4 Mullins effect model

Storage and loss moduli of viscoelastic material change with the strain amplitude. The greater the strain amplitude, the lower the storage modulus while the loss modulus has a peak at intermediate strain amplitude levels. Recent studies [20, 23] have shown

21

that rubber undergoes complicated rate and temperature effects when subjected to dynamic loading histories. Under cyclic loading, rubber shows hysteresis effects and energy losses during each deformation cycle [1]. Mullins effect [1] where the rubber material experiences significant softening during the initial cycles of loading but reaches a steady-state hysteresis after softening is very significant in rubber materials.

The Mullins effect is used with fully incompressible isotropic hyperelastic constitutive models and modifies the behavior of those models. The Mullins effect model is based on maximum previous load, where the load is the strain energy of the virgin hyperelastic material. As the maximum previous load increases, changes to the hyperelastic constitutive model due to the Mullins effect also increase. The modified Ogden-Roxburgh pseudo-elastic Mullins effect model [1] is used to simulate that effect in this study. The above model results in a scaled stress are given by;

$$S_{ij} = \eta S_{ij}^0 \tag{1.20}$$

where, η is the modified Ogden-Roxburgh damage variable. The functional form of the damage variable is;

$$\eta = 1 - \frac{1}{r} erf \left[\frac{W_m - W_0}{m + \beta W_m} \right] \tag{1.21}$$

where, W_m is the maximum previous strain energy and W_0 is the strain energy for the virgin hyperelastic material. η requires the three material constants r, m, and β which were assigned based on previous researchers' work [3], [4].

1.8.2 Dry friction model

1.8.2.1 Pavement modeling

Asphalt concrete pavements and concrete pavements have different texture patterns, as seen in Figure 1.6. Asphalt concrete pavements typically have aggregate particles exposed on the surface of the pavement representing macro level roughness.

Figure 1.6: Asphalt and concrete pavements

The micro level roughness is considered as the surface roughness of aggregates themselves. Concrete surfaces generally have a smoother surface in terms of macro level texture since concrete surfaces often have a smooth finish compared to asphalt concrete surfaces. However, some concrete surfaces may have joints and other concrete surfaces may be grooved in order to improve drainage capability and to increase the macro level texture. Therefore, the observed tire friction effects on such surfaces exhibit significant differences as well. The effect of surface roughness on adhesion for elastomer contact on rough surfaces has been studied in Fuller and Tabor [6]. They revealed that a relatively small surface roughness could remove the effect of adhesion and developed a simple model by assuming the surface roughness on a single length scale. The overall contact force was obtained by applying the JKR (Johnson, Kendall, Roberts) contact theory [7] to

each individual asperity.

There are two important scales to be considered; (1) the macro scale to model hysteretic friction due to the macro texture, and (2) the micro scale to represent micro hysteresis and adhesion. A schematic of the two scale models and how they interplay are shown in Figure 1.7. Obviously only one particular scale transition is not adequate to simulate the real road profile. The multi-scale approach is very important to determine the effects from micro-roughness of single asperities to macro-roughness of the road. Furthermore, a single hemispheric function is also not an accurate approximation for a rough surface.
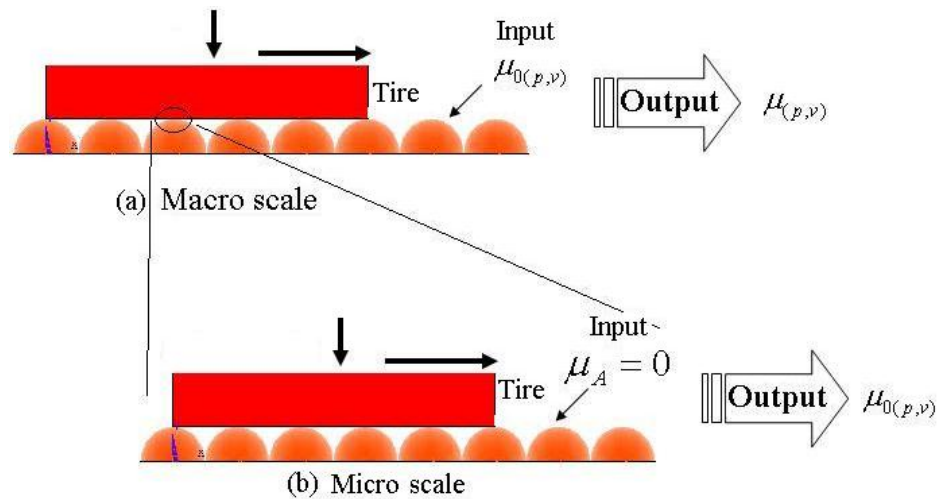
Figure 1.7: Micro scale and macro scale description

1.8.2.2 Tire modeling

In the preliminary study, the tire has been simulated as a small rubber block. A three dimensional model of a rectangular rubber block sliding over regularly spaced hemispheric roughness surface was developed as depicted in Figure 1.8.
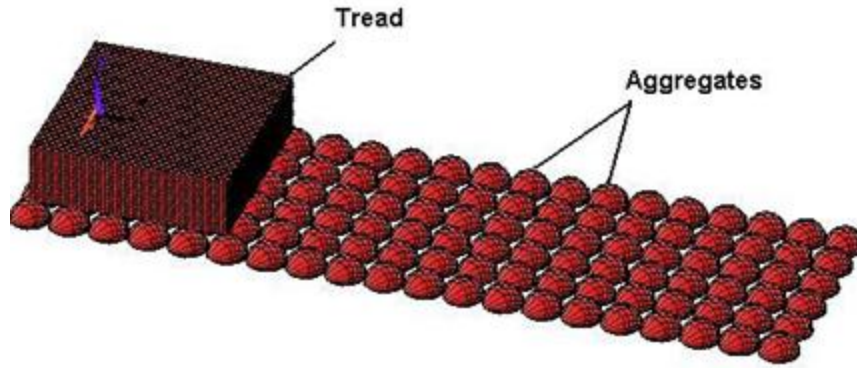
Figure 1.8: ANSYS finite element model of a sliding rubber block

1.8.2.2.1 Contact model

Surface to surface contact elements were used in this study since they are well suitable for detecting the gap between contact elements and target elements in the 3D finite element analysis. Since the pavement can be considered as rigid and the tire surface can be considered as flexible, the pavement surface elements are considered as rigid target elements and the bottom surface elements of the rubber block are considered as flexible contact elements.

ANSYS contact element was used as the ANSYS contact element type which is capable of changing the coefficient of friction with temperature, time, normal pressure, sliding distance or sliding relative velocity. ANSYS target element type was used as the target elements. The target surface is modeled through a set of target segments with typically, several target segments comprising one target surface. Each target surface can be associated with only one contact surface, and vice-versa. However, several contact elements could make up the contact surface and thus come in contact with the same target surface.

Augmented-Lagrangian method is used as the contact algorithm. In this the contact tractions (pressure and frictional stresses) are augmented during equilibrium

iterations so that the final penetration is smaller than the allowable tolerance. The coefficient of friction (μ) is defined using the Coulomb friction model. μ can depend on the temperature, time, normal pressure, sliding distance, or sliding relative velocity. The maximum contact friction stress can be introduced so that, regardless of the magnitude of normal contact pressure, sliding will occur if the friction stress reaches this value. Another real constant used for the friction law is the cohesion which provides sliding resistance even with zero normal pressure. Usually, the static μ value is higher than the dynamic μ value.

1.8.2.3 Contact detection

As depicted in Figure 1.9, contact detection points are located at the Gauss integration points of the contact elements which are interior to the element surface. The contact element is constrained against penetration into the target surface at its integration points. ANSYS surface-to-surface contact elements use Gauss integration points as a default, which generally provide more accurate results than the nodal detection scheme, which uses the nodes themselves as the integration points.
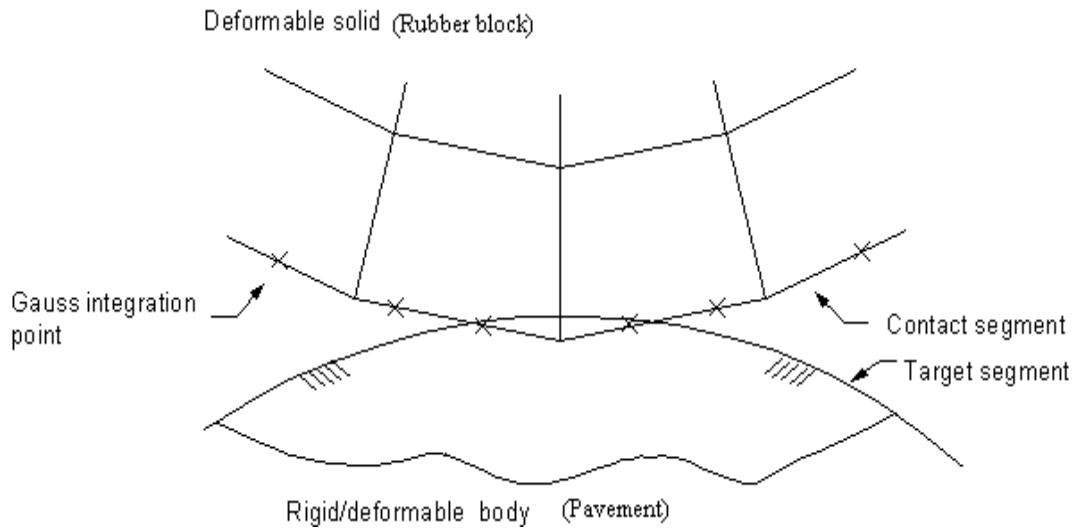
Figure 1.9: Contact detection located at Gauss integration point

The contact detection occurs based on a defined pinball region as shown in Figure 1.10. Each target element has a pinball region and the program checks for contact elements and detects whether it is outside the pinball, inside the pinball and how far it is from the target. Then it passes the signal to the contact algorithm regarding the contact condition so that the program is able to perform the contact analysis based on the contact condition.
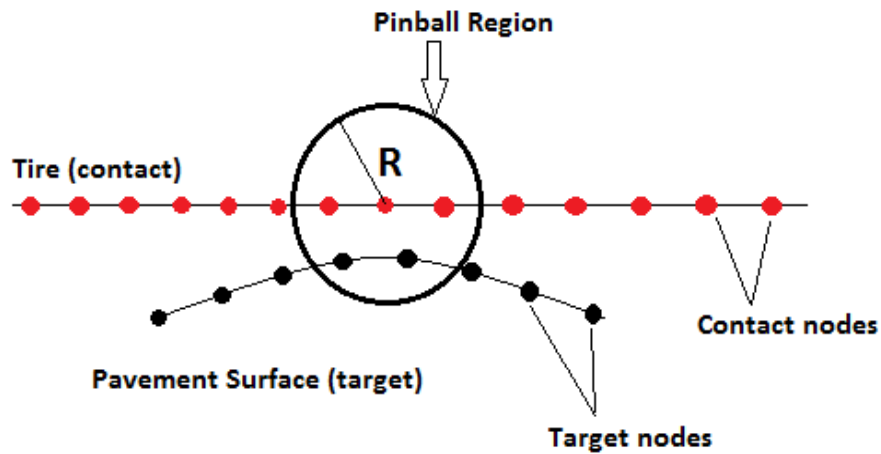
Figure 1.10: Pinball region

1.8.2.4 Details of the macro scale model

The rubber block dimensions at the macro scale were 50 mm, 50 mm and 10 mm in length width and height. The model has been verified with dry friction test results obtained by the Locked wheel skid tester. For this purpose, three tests were performed at three different speeds of 30, 40 and 50 mph at the standard tire pressure of 24 psi at a selected site. Then three additional tests were performed at three different tire pressures of 16, 24 and 32 psi at the standard speed of 40 mph at the same site. The area under the test tire was measured at each tire pressure tested in order to calculate the average vertical pressure at the tire-pavement contact. The Micro-Texture Depth (MTD) of the tested pavement was observed to be 0.40 mm by performing a CT Meter test. The MTD is a

widely used texture parameter which represents the average texture depth of a certain profile. Generally, two different profiles with the same MTD can be expected to respond similarly when a tire slides. Hence, the FE program results were predicted with the MTD of the hemispheric surface being equal to the MTD measured in the field.

Figure 1.11: Speed vs. coefficient of friction
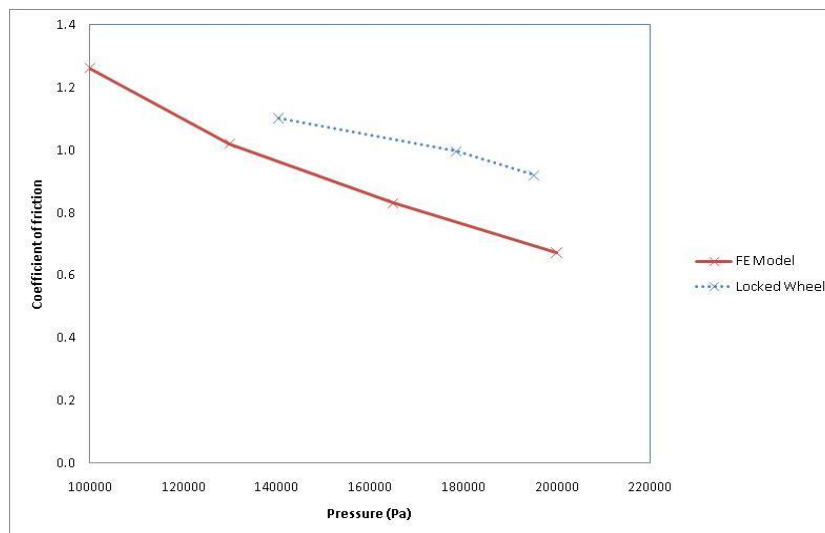
Figure 1.12: Average vertical pressure vs coefficient of friction

According to Figure 1.11 both the field results as well as FE model results have slightly increasing trends of the coefficient of friction with the speed. Similarly the FE predictions and the field measurements in Figure 1.12 show a considerable decrease in the coefficient of friction with the vertical pressure. However, in both Figures 1.11 and 1.12 the coefficients of friction in the field are to be higher than the FE Model results. The possible reasons for the observed difference could be as follows;

- Simple rubber block used to represent a tire does not consider the pressure distribution on the tire patch, tire composition such as the carcass, tire geometry etc.

- Finer meshes of FE model give more accurate results and increase computational effort. Due to the limitations of available computer resources, the number of nodes in the FE model i.e. the accuracy level, is limited.

- Coefficient of friction was calculated based on the assumption that the entire energy loss contributes to generate friction without considering thermal or any other losses. However the energy loss due to abrasion is considerable under the dry condition.

- Inaccuracies of the modeled properties of SBR since the material properties of SBR were assigned based on previous researchers' work.

- Discounting of adhesional friction whereas the adhesional friction has considerable effects on dry friction on rough surfaces as discussed in Section 1.

- The assumption that two different profiles with the same MTD can be expected to respond similarly when a tire slides, is not exactly applicable when an extremely irregular surface is compared with a simple hemispheric surface. The irregularities do not always affect the overall MTD but they would certainly affect the hysteretic friction.

All in all it can be considered that, without considering complex conditions like adhesional friction and randomization of the pavement profile, the FE model has produced field coefficients of friction that are agreeable with field measurements.

Measurement of micro-texture of a selected pavement is a complicated task. Therefore a micro scale model was not developed and the multi scale approach was not performed in the preliminary study. However, a FE model was developed for an arbitrarily selected micro scale model with hemispheric diameter of 0.5 mm. The model was subjected to the same loading conditions as those at the macro level model. Figures 1.13 and 1.14 follow similar trends as Figures 1.11 and 1.12. However, the values of coefficient of friction in Figures 1.13 and 1.14 are lower than in Figures 1.11 and 1.12. This observation justifies the fact that micro level hysteresis energy losses are lower than macro level hysteresis energy losses.

1.8.3 Viscous hydroplaning model

This section deals with the modeling of a rubber block sliding on a pavement with partially soaked asperities. The thickness of the water layer that contributes to dynamic hydroplaning is the Mean Texture Depth (MTD) and the thickness of the water film above the tops of the surface asperities. The thickness of the water layer that contributes to viscous hydroplaning is the total texture depth i.e. the distance from the tops of the asperities to the bottoms of the asperities, minus the MTD. Even though the real hydroplaning situation in the field is a combination of viscous and dynamic hydroplaning, the initial work is only targeted to model viscous hydroplaning. Dynamic hydroplaning will be modeled in a later stage.
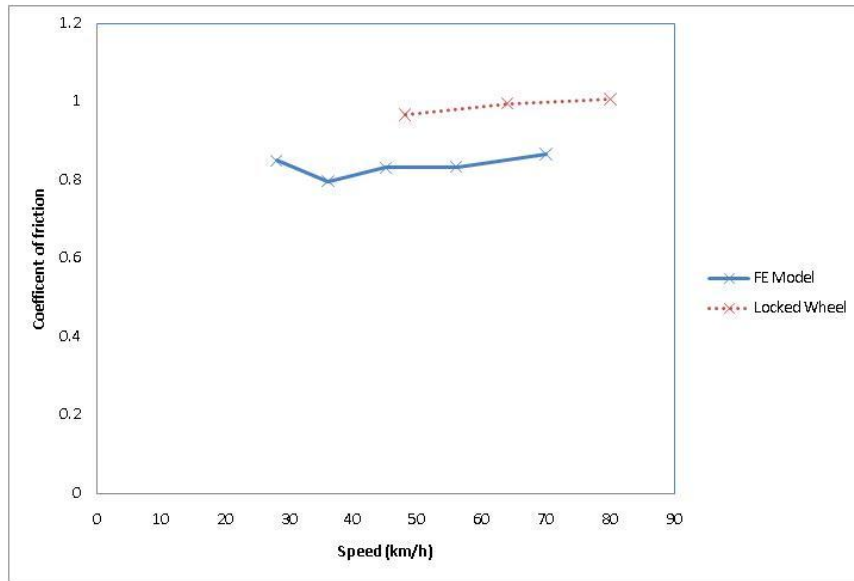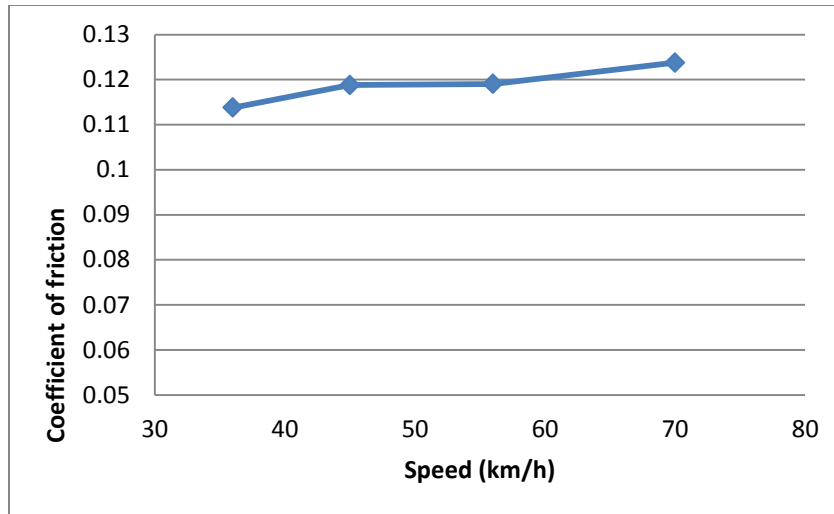
Figure 1.13: Speed vs. coefficient of friction
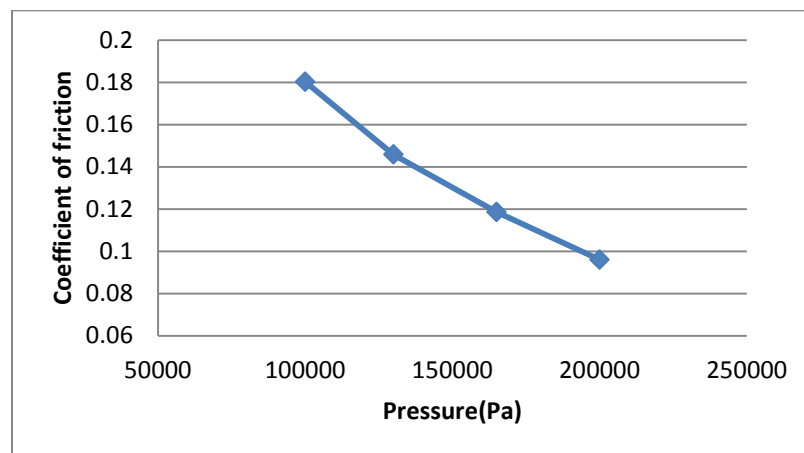
Figure 1.14: Average vertical pressure vs. coefficient of friction

Under this situation the model will be able to represent the entrapped water or any other contaminations in the asperities. The entrapped water can be considered as incompressible and acting as a frictionless rigid surface. In other words, it acts as a sealant to asperities and reduces the draping effects and hysteretic friction.

Figure 1.15 shows a three dimensional view of the Finite Element model. Diameter of the hemispheres was assigned such that the MTD of the hemispheric surface

is equal to the MTD of a real pavement measured by CT Meter test. In the illustrative example the diameter of the hemispheres were set to be 2.0 mm. In order to explore the effect of entrapped water depth on friction, the water depth has been varied at a certain pressure (80,000 Pa) and a speed of 60 km/h. Figure 1.16 indicates that the water depth has a very significant effect on hysteretic friction.
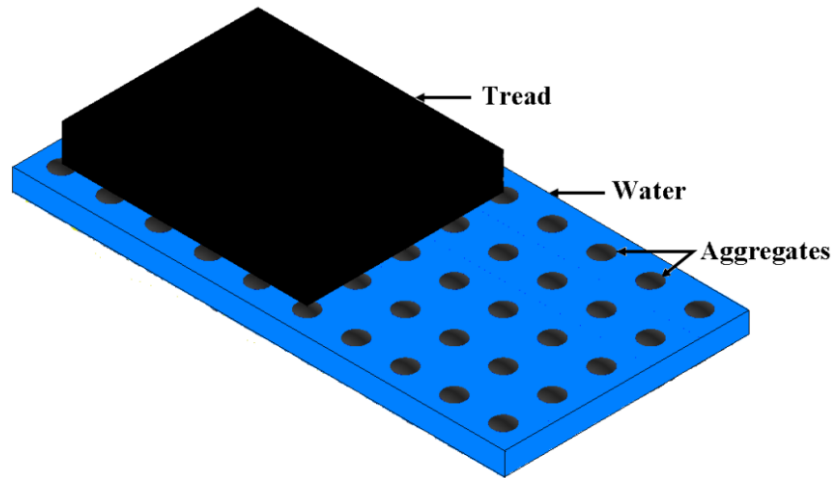
Figure 1.15: ANSYS finite element model of a sliding rubber block

Then the effect of vertical pressure on hysteretic friction was considered for a given water depth of 1.7 mm a speed of 60 km/h. Figure 1.17 shows the predicted results.
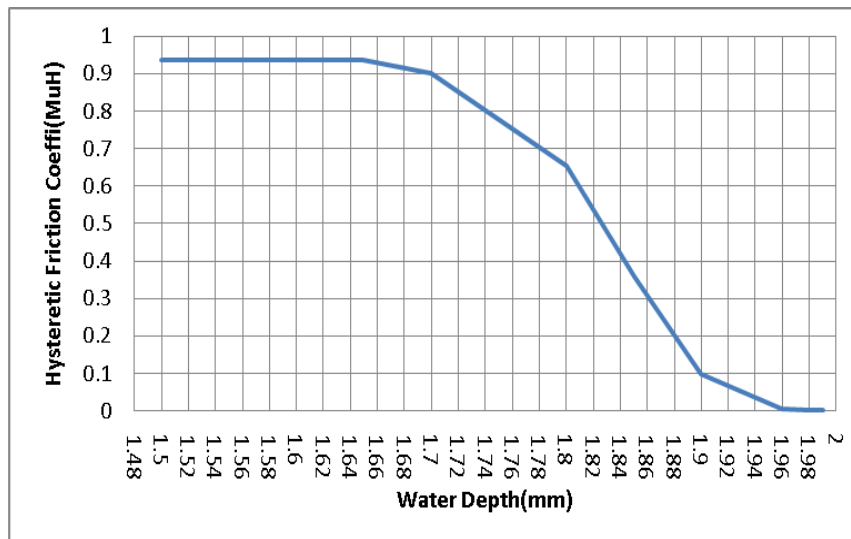
Figure 1.16: Effect of water depth on coefficient of hysteretic friction
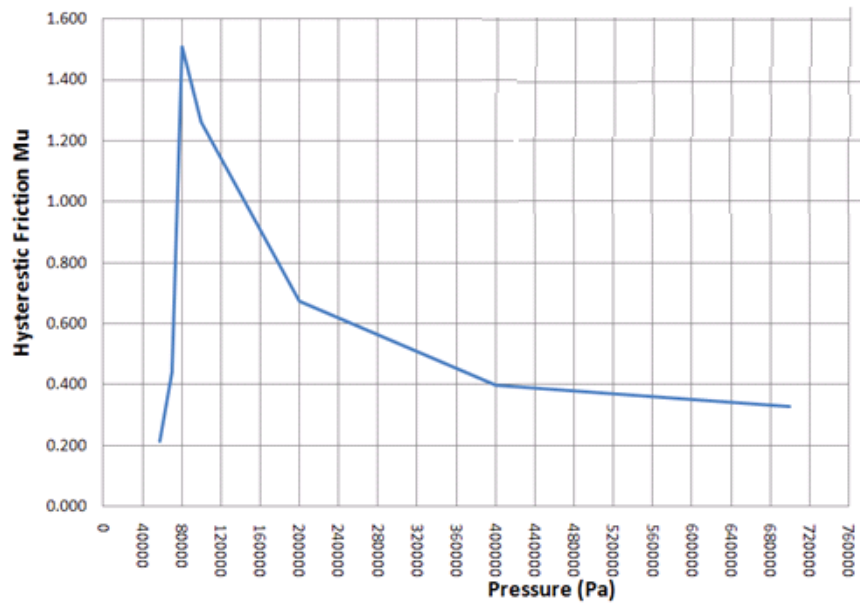
Figure 1.17: Effect of vertical pressure on coefficient of hysteretic friction

CHAPTER 2

SLIDING FRICTION OF A SMOOTH TIRE ON A ROUGH MOIST PAVEMENT
SURFACE – EVALUATION OF TWO PREDICTION METHODS

2.1 Introduction

The study and evaluation of tire-pavement friction have drawn renewed interest

during the last few decades because of the need for effective friction rehabilitation on

highways and runways mandated by stringent friction management programs. However,

accurate prediction of friction on wet pavements that leads to vehicle skidding is still a

partially solved problem involving a multitude of factors such as tire inflation pressure,

sliding or rolling speed, vertical load, geometry, cross-sectional properties, material

properties and pavement surface texture characteristics. The available tire-pavement

friction models can be divided into two categories as static friction models and dynamic

friction models. Static friction models are appropriate for steady-state operating

conditions; the most widely used one being the Pacejka's magic formula [1]. On the other

hand, the dynamic tire models become more accurate when a tire is under braking or

acceleration. Although relatively more accurate dynamic models have been developed

recently those models are not any more capable of modeling the influence of the

geometric and material properties of the tire and texture properties of the pavement on the

tire-pavement friction interaction than the prediction tools that had existed. The Dhal

model, bristle model and Lugre model are some examples of dynamic friction models [1,

2, 3]. The motivation behind the current work is the need for accurate and reliable

34

predictive tools of tire pavement friction particularly under the more critical moist conditions caused by wet weather. Therefore, the work reported in this chapter is concerned with the development of a numerical model and an analytical model for predicting the sliding friction of a smooth tire on a rough moist pavement surface and comparison of the corresponding predictions with the results of field experiments. The proposed numerical model (based on finite element software ANSYS) has the capability of simulating pavement macrotexture characteristics, tire geometric and material properties, tire pressure, vertical loading and sliding of the tire and it can be used to evaluate the hysteretic friction under steady state sliding conditions. On the other hand, the proposed analytical tire model can directly predict the hysteretic friction of a sliding tire on a random rough pavement surface based on fundamental concepts of hysteresis.

2.1.1 Pavement texture

The texture of a road surface plays a significant role in the development of tire friction. Surface roughness is generally classified into three length scales; (1) micro, (2) macro and (3) mega texture. Micro and macro texture are the respective regimes where characteristic texture dimensions are less than 0.5 mm and lie in the range of 0.5 mm to 50 mm. Texture levels greater than 50 mm (megatexture) does not contribute to conventional friction and only causes vibration of the vehicle suspension systems. Texture levels below the micro level can be excluded since dust and dirt particles generally fill the asperities below the micro level, making them irrelevant to generation of significant friction.

2.1.2 Components of pavement friction

The two major independent mechanisms which contribute to sliding friction of rubber are adhesion and hysteresis. Adhesion friction depends on the intermolecular-kinetic, thermally activated stick-slip mechanism which takes place essentially at the sliding interface. Elastomer structures like rubber are composed of flexible molecular chains and during relative sliding between an elastomer and a rigid surface, the polymer chains in the elastomer slide relative to each other forming and breaking local bonds, leading to an energy loss. Thus, it is the pavement microtexture that contributes mostly to adhesion. On the other hand, hysteretic friction depends on the viscoelastic characteristics of rubber and depends directly on the energy dissipation inside the material due to the frequency of indentation by the pavement macrotexture. The existence of varying roughness levels on a given pavement yields a considerable range of indentation frequencies during the sliding maneuver. According to Moore [4], adhesion friction peaks occur at lower sliding velocities while hysteretic friction peaks occur at higher sliding velocities. Since adhesion plays an insignificant role in producing friction on moist surfaces, this component of friction is not considered in this study.

2.1.3 Pavement moisture condition

This study differs from a typical wet pavement friction study as it only focuses on moist pavement conditions. According to the American Concrete Pavement Association's (ACPA's) [30] definitions moist condition is slightly damp but not quite dry to the touch; the term "wet" implies visible free water while "damp" implies less wetness than "wet". In this condition pavement surface characteristics change at the molecular scale by absorbing water and therefore decreasing intermolecular bonds i.e. adhesive bonds

between the pavement surface and tire. The authors were able to simplify this extremely complex problem by neglecting the adhesion friction in this study. Adhesion is not expected to significantly contribute to friction of a sliding tire on a slightly wet or a contaminated surface. According to past researchers it has been found that the adhesion friction is insignificant for a tire sliding on a contaminated pavement surface since adhesion is predominant on uncontaminated dry surfaces at very small sliding speeds [17, 27, 28, 29].

2.1.4 Field experiments

2.1.4.1 Locked Wheel Skid Tester (LWST) tests

Locked Wheel Skid tests are typically performed under wet conditions. However, since this study focuses on moist condition, the experiment was arranged to moisten a completely dry asphalt pavement surface. This condition was obtained by moistening the pavement test path with a wet sponge just before performing each LWST test. The water nozzle which supplies water for a typical LWST test was blocked to prevent any additional water to drop on the pavement. The tests were performed for 30, 40 and 50 mph at the standard tire pressure of 24 psi and load of 1085 lb at a selected site. And each test was repeated five times on a fresh test path in order to maintain the moist condition. Based on the discussion in section 2.1.3, in the above tests the field manifested friction can be assumed to be only due to hysteretic friction.

2.1.4.2 Circular Texture (CT) meter tests

The CT meter can be used to evaluate the macrotexture profile on pavement surfaces with a laser profiler which travels circumferentially. Since the CT meter profile

is being measured circumferentially, the statistical properties estimated by those height measurements are representative of all directions on the pavement surface. Therefore, CT meter tests were performed on each LWST test location repeatedly and statistical properties (mean, standard deviation and frequency distribution of the heights) were evaluated. Since the profile measurements are representable to all the directions on the pavement, those statistical properties have been used to generate a three dimensional random surface in the study.

2.2 Development of the numerical model

A numerical model of a smooth test tire of the Locked Wheel Skid Tester (LWST) sliding on a randomly rough moist pavement surface was developed using ANSYS 12.0 software. The details of the developed numerical methodology are discussed in the following sub-sections.

2.2.1 Tire geometric model

The LWST uses an ASTM E524-08 standard smooth tire for pavement skid-resistance tests. In this research, a 3-dimensional numerical model of this tire was developed using the relevant geometrical and cross sectional properties evaluated by slicing a spent standard tire. The tire model was developed in Solid Works 2010 software and imported to the ANSYS platform. This tire has two belted plies, two biased plies and beads. A sectional view of the locked wheel tire cut and developed in Solid Works 2010 is depicted in Figure 2.1(a) and Figure 2.1(b) respectively.
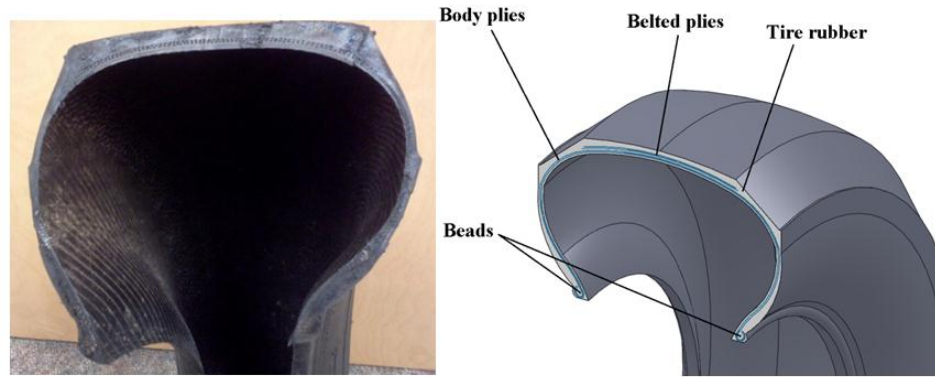
Figure 2.1: Sectional views of (a) the standard tire (b) the tire geometry

2.2.2 Tire material model

The LWST standard tire consists of four different materials. Tire rubber, the major tire component contributing to friction, usually consists of Styrene Butadiene Rubber (SBR) and belted plies and body plies are made of fiberglass and a polyester material respectively while the beads contain steel. The relevant material properties were obtained from previous researches ([5], [6]). Tire rubber exhibits hyperelastic and viscoelastic (hyper-viscoelastic) characteristics. ANSYS software has the capability of modeling hyperelastic material with the Mooney-Rivlin material model [7] and viscoelastic material with the Prony series material model [8]. Therefore a combined Mooney-Rivlin and Prony series model was developed in ANSYS to model the hyper-viscoelastic rubber. At the pavement asperity contacts, tire rubber is subjected to alternating draping and undraping into and out of the pavement texture. Under this cyclic loading, in each deformation cycle rubber undergoes a viscoelastic energy dissipation governed by the loss modulus of rubber. The loss and storage moduli (E// and E/) of rubber material change with the excitation amplitude and frequency. Brief descriptions of the constitutive equations used in Mooney-Rivlin and the Prony series material models are given in the Section 1.8.1.2.2 and 1.8.1.2.3 respectively.

2.2.3 Pavement model with random roughness

The randomness of texture on pavement surfaces makes the modeling of rough pavements a tedious task and therefore, no significant evidence was found in the literature on such studies. The authors introduced a novelty by modeling a rough pavement in ANSYS software based on texture properties of a selected pavement surface evaluated by a Circular Texture (CT) meter. The CT meter can be used to evaluate the macrotexture profiles on pavement surfaces with a laser profiler which scans the pavement surface circumferentially. Since measurement of the surface profile heights is performed at 0.87 mm spacing, the CT meter is incapable of measuring the microtexture. Moreover, due to the impracticality of having an adequately fine mesh, one limitation of numerical models is that they are only capable of modeling macro-hysteretic friction. The above limitations do not affect the current work since friction originating from microtexture (adhesion) is negligible on moist surfaces. In this work, the mean and the standard deviation of the distribution of the macrotexture heights of the tested pavement (Figure 2.2(a)) were used to generate a random surface in ANSYS. Then, this random surface was input to the numerical program and meshed as seen in Figure 2.2(b).

It must be noted that the summits of the generated random surface have to be smoothened in order to prevent the development of excessive pressures/displacements at the summits where the tire contacts the pavement surface, and the consequent failure of the analysis. Since the pavement surface summits were smoothened in the numerical model, the generated pavement model can be considered as only a simplified model of the tested pavement surface. Figure 2.3 shows the combined tire and pavement numerical model.
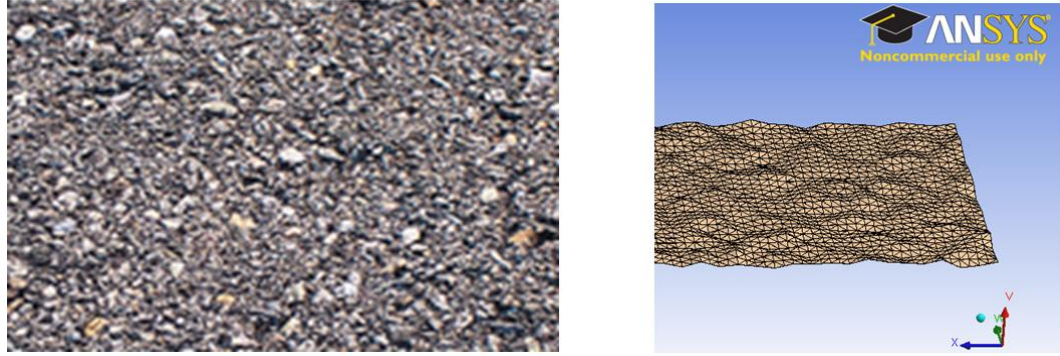
Figure 2.2: (a) Tested asphalt pavement (b) numerical model surface
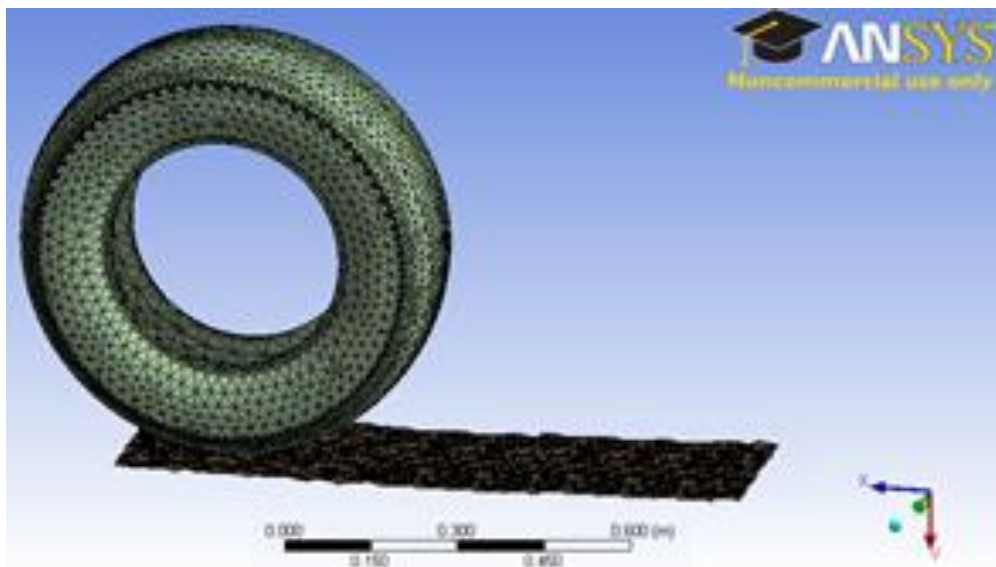
Figure 2.3: Tire and pavement numerical model

2.2.4 Implementation of ANSYS numerical model

In the numerical model, the pavement was considered to be rigid while eight nodded hexagonal solid element was used to model the solid rubber elements defined by eight nodes and orthotropic material properties which are unique and independent in the directions of three mutually perpendicular axes. This element is capable of representing hyperelastic and viscoelastic material properties in the model. The default element coordinate system is along the global directions defined based on a, x, y, z global

Cartesian coordinate system. The origin of the x, y, z coordinate system is a fixed arbitrary point on the tire close to the pavement.

2.2.4.1 Finite element formulation

Nodes and elements move with the material in Lagrangian meshes while interfaces and boundaries remain coincident with element edges. Therefore the constitutive equations are always evaluated at the same material point and it is advantageous for history dependent materials.

SBR rubber material simulated in the finite element model is nonlinear and it is subjected to large deformations. Updated Lagrangian formulation is used in the finite element model where the derivatives are with respect to the spatial (Eulerian) coordinates and the weak form involves the integration over the deformed configuration. As discussed in this section later, the momentum equation, which is expressed in terms of Eulerian (spatial) coordinates and the Cauchy (physical) stress, has been discretized in this formulation. Then a weak form of the momentum equation which is known as the principle of virtual power is derived where the derivatives are with respect to special coordinates, i.e. on the current configuration. As shown in Figure 2.4, a body which occupies a domain Ω with a boundary Γ has been considered. The governing equations for the mechanical behavior of a continuous body are;

1. Conservation of mass as shown in Equation 2.1

$$\rho(\mathbf{X})J(\mathbf{X}) = \rho_0(\mathbf{X})J_0(\mathbf{X}) = \rho_0(\mathbf{X}) \qquad (2.1)$$

2. Conservation of linear momentum and angular momentum as shown in Equation 2.2 and 2.3 respectively;

42

$$\frac{\partial \sigma_{ji}}{\partial x_j} + \rho b_i = \rho \dot{v}_i \equiv \rho \frac{Dv_i}{Dt} \tag{2.2}$$

$$\sigma_{ij} = \sigma_{ji} \tag{2.3}$$

3. Conservation of energy as shown in Equation 2.4;

$$\rho \dot{w}^{int} = \mathbf{D}{:}\sigma - \nabla \cdot \mathbf{q} + \rho s \quad \text{or} \quad \rho \dot{w}^{int} = D_{ij}\sigma_{ji} - \frac{\partial q_i}{\partial x_i} + \rho s \tag{2.4}$$

4. Constitutive equations as shown in Equation 2.5;

$$\sigma^{\nabla} = S_t^{\sigma D}(\mathbf{D}, \sigma, \text{etc.}) \tag{2.5}$$

5. Strain-displacement equations as shown in Equation 2.6;

$$D_{ij} = \frac{1}{2}\left(\frac{\partial v_i}{\partial x_j} + \frac{\partial v_j}{\partial x_i}\right) \tag{2.6}$$

Here the dependent variables are the velocity $v(X, t)$, the Cauchy stress $s(X,t)$, the rate-of deformation $D(X,t)$ and the density $r(X,t)$. The boundary conditions are summarized in Equation 2.7;

$$\mathbf{v}(\mathbf{x},0) = \mathbf{v}_0(\mathbf{x}) \qquad \sigma(\mathbf{x},0) = \sigma_0(\mathbf{x}) \tag{2.7}$$
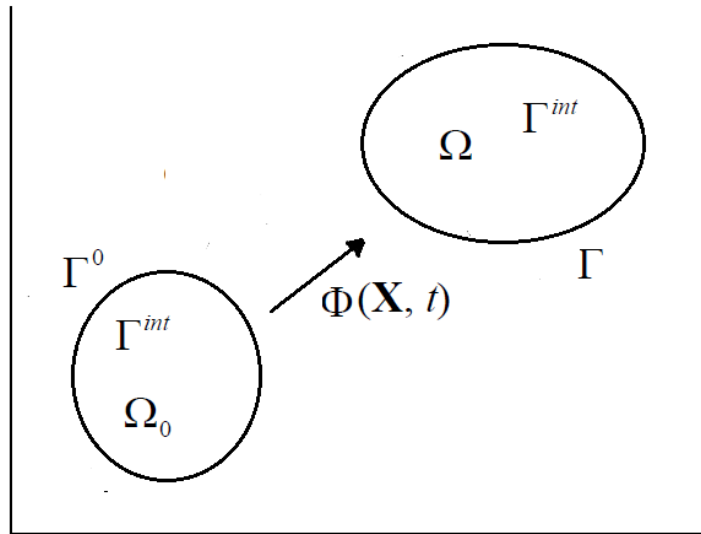
Figure 2.4: Reference and deformed configuration

The principle of virtual power which is the weak form of the momentum equation, traction boundary conditions and the interior traction continuity equation have been derived for the updated Lagrangian formulation. If σ_{ij} is a smooth function of the displacements and velocities and $v_i \in U$;

$$\frac{\partial \sigma_{ji}}{\partial x_j} + \rho b_i = \rho \dot{v}_i \quad \text{in } \Omega \tag{2.8}$$

$$n_j \sigma_{ji} = \bar{t}_i \quad \text{on } \Gamma_{ti} \tag{2.9}$$

$$\left(n_j \sigma_{ji} \right) = 0 \quad \text{on } \Gamma_{int} \tag{2.10}$$

where, the total virtual internal power δP^{int} is defined by the integral of $dD_{ij}\sigma_{ij}$ over the domain;

$$\delta P^{int} = \int_\Omega \delta \mathbf{D} \boldsymbol{\sigma} \, d\Omega = \int_\Omega \delta D_{ij} \sigma_{ij} \, d\Omega = \int_\Omega \frac{\partial (\delta v_i)}{\partial x_j} \sigma_{ij} \, d\Omega \tag{2.11}$$

The virtual external power δP^{ext} is defined where the virtual external power arises from the external body forces $\mathbf{b}(\mathbf{x}, t)$ and prescribed tractions $\mathbf{t}(x,t)$;

$$\delta P^{ext} = \int_\Omega \delta \mathbf{v} \cdot \rho \mathbf{b} d\Omega + \sum_{j=1}^{n_{SD}} \int_{\Gamma_{tj}} \left(\delta \mathbf{v} \cdot \mathbf{e}_j \right) \bar{\mathbf{t}} \cdot \mathbf{e}_j d\Gamma = \int_\Omega \delta v_i \rho b_i d\Omega + \sum_{j=1}^{n_{SD}} \int_{\Gamma_{tj}} \delta v_j \bar{t}_j d\Gamma \tag{2.12}$$

And the virtual inertial power which is the power corresponding to the inertial force is defined by;

$$\delta P^{inert} = \int_\Omega \delta \mathbf{v} \cdot \rho \dot{\mathbf{v}} d\Omega = \int_\Omega \delta v_i \rho \dot{v}_i d\Omega \tag{2.13}$$

2.2.4.2 Updated Lagrangian finite element discretization

The finite element equations for the updated Lagrangian formulation are discretized by subdividing the current domain Ω into elements Ω_e. The nodal coordinates in the current configuration are defined by x_{iI}, $I = 1$ to n_N. Lower case subscripts are

used for components and upper case subscripts for nodal values. In the finite element method, the motion $x(X, t)$ is approximated by;

$$x_i(\mathbf{X},t) = N_I(\mathbf{X})x_{iI}(t) \tag{2.14}$$

where, $N_I(\mathbf{X})$ are the interpolation (shape) functions and $\mathbf{x}_I$ is the position vector of node I. By considering a three dimensional isoperimetric element, the motion of the element is given by;

$$\begin{Bmatrix} x \\ y \\ z \end{Bmatrix} = N_I(\xi) \begin{Bmatrix} x_I(t) \\ y_I(t) \\ z_I(t) \end{Bmatrix} \tag{2.15}$$

where, and $N_I(\xi)$ are the shape functions. The deformation gradient can be defined by;

$$\mathbf{F} = \frac{\partial \mathbf{x}}{\partial \mathbf{X}} = \mathbf{x}_I N_{I,X} = \mathbf{x}_I N_{I,\xi}^T \mathbf{X}_{,\xi}^{-1} \equiv \mathbf{x}_I N_{I,\xi}^T \left(\mathbf{F}_\xi^0 \right)^{-1} \tag{2.16}$$

where,

$$\mathbf{X}_{,\xi} \equiv \mathbf{F}_\xi^0 = \mathbf{X}_I N_{I,\xi}^T \tag{2.17}$$

The internal nodal forces are obtained by Equation 2.18 and the external nodal forces are defined by Equation 2.19;

$$\left(\mathbf{f}_I^{Int}\right)^T = \left[f_{xI}, f_{yI}, f_{zI}\right]^{Int} = \int_\Omega B_I^T \sigma d\Omega = \int_\Delta \begin{bmatrix} N_{I,x} & N_{I,y} & N_{I,z} \end{bmatrix} \begin{bmatrix} \sigma_{xx} & \sigma_{xy} & \sigma_{xz} \\ \sigma_{xy} & \sigma_{yy} & \sigma_{yz} \\ \sigma_{xz} & \sigma_{yz} & \sigma_{zz} \end{bmatrix} J_\xi d\Delta \tag{2.18}$$

$$f_{iI}^{ext} = \int_\Omega N_I \rho\, b_i d\Omega = \int_\Delta N_I(\xi)\rho(\xi)b_i(\xi)J_\xi d\Delta \tag{2.19}$$

$$\begin{Bmatrix} f_{xI} \\ f_{yI} \\ f_{zI} \end{Bmatrix}^{ext} = \int_{-1}^{1}\int_{-1}^{1}\int_{-1}^{1} N_I(\xi)\rho(\xi) \begin{Bmatrix} b_x(\xi) \\ b_y(\xi) \\ b_z(\xi) \end{Bmatrix} J_\xi d\xi d\eta d\zeta \tag{2.20}$$

For a pressure load, only the normal component of the traction is nonzero. The nodal external forces are then given by Equation 2.21 and the integral has been evaluated over the loaded surface of the tire element.

$$f_{iI}^{ext} = \int_\Gamma t_i N_I d\Gamma = -\int_\Gamma p n_i N_I d\Gamma = -\int_{-1}^{1}\int_{-1}^{1} p\, e_{ijk} x_{j,\xi} x_{k,\eta} N_I d\xi d\eta \quad (2.21)$$

2.2.4.3 Contact model

Contact model has the formulation of Augmented Lagrangian Eulerian formulation which is similar to the Updated Lagrangian formulization. However, in contrast to the updated Lagrangian method the state variables are written in terms of the referential coordinates. At the end of each time step the referential situation is updated with the current situation. In this algorithm, the contact stresses are augmented during equilibrium iterations so that the final penetration is smaller than the allowable tolerance value which can be defined in the analysis.

2.2.4.3.1 Augmented Lagrangian solution algorithm

The detailed algorithm to solve the contact analysis must follow several iterative steps and those steps are given below;

1. Initialization;

   a. Decide the number of load steps τ (choose the load increment Δt)

   b. Initialize the tangential stiffness matrix $\overline{K}^{(0)} + \overline{K}_c^{(0)}$

   c. Set the parameters $\overline{K}_n^{(0)} > 0, \overline{K}_t^{(0)} > 0$ K_n and K_t are penalty parameters correspond to the constrains.

2. Increase load step to $t+\Delta t$. Find the external load at step $t+\Delta t$;

   a. Start the augmentation loop.

b. Assign initial conditions for the current step.

c. Minimize the augmented Lagrangian function.

3. This step solves the Newton−Raphson equation iteratively while keeping the ALM parameters fixed. The following are the sub steps:

a. Solve the Newton−Raphson equation to obtain incremental displacement.

b. Evaluate the normal penetration.

c. Calculate the contact force vector and the contact stiffness matrices for nodes.

d. Compute the tangent stiffness matrix and the internal force vector.

e. Repeat the steps until the penetration is less than or equal to the tolerance.

Surface to surface contact elements were used at the rubber and pavement interface since they are well suited for detecting the gaps between contact elements (rubber) and target elements (pavement) in the 3D numerical analysis. Since the pavement and the tire surface are considered as rigid and flexible respectively, the pavement surface elements are assumed to be rigid target elements and the bottom surface elements of the rubber tire are assumed to be flexible contact elements. ANSYS contact element was used as the ANSYS contact element type. The target surface was modeled with segments of target elements. Each target surface can be associated with only one contact surface and vice-versa. However, numerous contact elements could make up the contact surface and thus come in contact with the same target surface. Contact detection points are located at the integration points of the contact elements. The contact element is constrained against penetration into the target surface at its integration points. ANSYS surface-to-surface contact elements use Gauss integration points [7]. A similar solution algorithm has been used in previous studies [1].

2.2.4.4 Loading procedure

First, the tire was inflated and completely loaded at its upper face by the standard LWST load of 1085 lb, which was kept constant during the sliding process. Then the tire was translated horizontally with a designated constant velocity. The friction values were evaluated in the steady-state sliding phase because such friction estimates can be expected to be more reliable compared to those of transient conditions.

2.2.5 Results of the numerical model

Statistically stationary conditions of the pavement surface texture properties were assumed to evaluate homogenized frictional stresses along the sliding direction. Therefore, it was possible to average the frictional stresses within an appropriately selected sliding distance. This distance was considered to be larger than ten times the largest aggregate size on the pavement.

The change in energy of the tire during the sliding motion was first evaluated without using viscoelastic properties. Then the change in energy during the same sliding distance was re-evaluated with viscoelastic properties. Thereafter, the energy dissipation due to hysteretic energy was determined from the difference between the above two computations.

2.2.5.1 Comparison of the numerical model results with field results

The FE model discussed in Section 2 was verified with friction test results obtained by the Locked wheel skid tester. For this purpose, three field skid tests were performed at three speeds of 30, 40 and 50 mph at the standard tire pressure of 24 psi and load of 1085 lb at a selected site. The above LW tests were performed under moist

pavement conditions without flooding the pavement like in typical LWS tests. The moisturization of pavements is expected to reduce adhesional friction by preventing the formation of adhesional bonds between tires and pavement surfaces. When the amount of moisture on a pavement increases the adhesional friction starts to decrease immediately and it will become almost zero at certain moisture content. However, hysteresis friction remains unchanged until water starts to stagnate on asperities and restricts draping of rubber thus initiating the condition of hydroplaning. Therefore, optimum moisture condition that was sought after in this test is the condition where the moisture content is sufficient to keep the adhesional friction negligible with no restriction on hysteresis friction. It was extremely difficult to determine this optimum moisture content due to the incapability of separately measuring adhesional and hysteresis friction components in the field. Therefore, the optimum moisture level which prevents the development of adhesion while avoiding viscous hydroplaning was determined by trial and error and maintained during the field tests. In a typical wet friction test, friction decreases with increasing sliding speed because when sliding speed increases the amount of water entrapped between the tire and pavement increases and causes to reduce friction. However, in this study under moist condition, friction is dominated by hysteresis effect which initially increases with speed and after a particular speed decreases.

The FE model discussed in Section 2 has been verified with friction test results obtained by the Locked wheel skid tester. Figure 2.5 shows a comparison of numerical model results with field test results. Although both curves have similar increasing trends the magnitudes are significantly different from each other. The numerical analysis was performed based on some assumptions. Among them, the tire rubber properties used in

this model are not the ones specific for LWST test tire. Also as explained in Section 2.4, smoothening of the summits in the numerical study makes the pavement surfaces in the field and the model different. The discrepancies could cause a positive or a negative total effect on the outcome. Therefore, it is extremely difficult to justify the outcome of this comparison without overcoming the above discrepancies. According to the discussion in Section 2.1.3, this study is not a typical we friction study and the results cannot be compared with the previous wet friction study results.
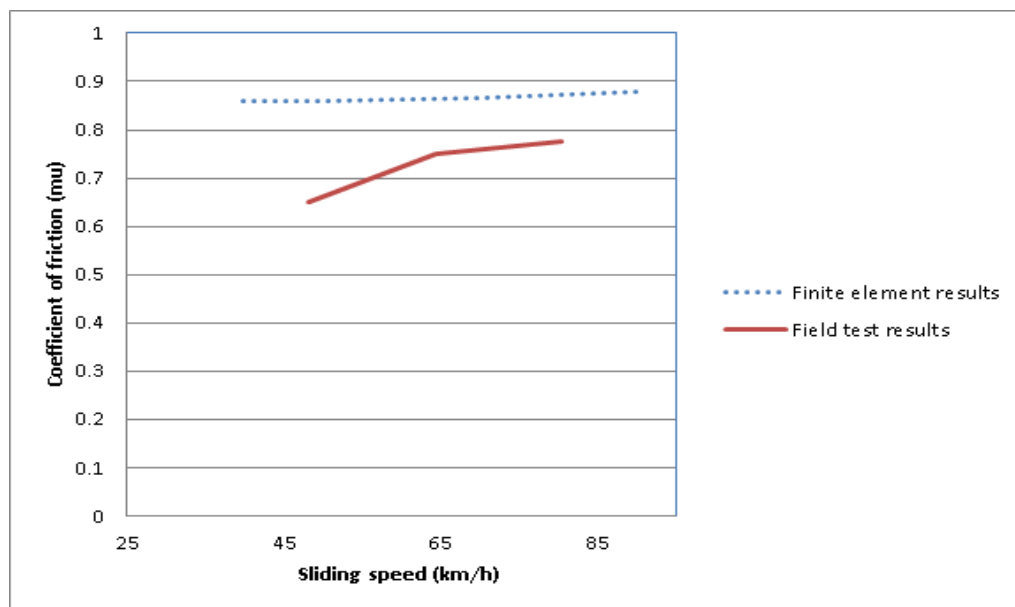
Figure 2.5: Comparison of numerical predictions of friction with field results

2.3 Development of the analytical model

In order to formulate an alternative but simpler analytical solution for this case, the Kluppel's concept [11], which has been developed to evaluate sliding friction of rubber, was applied to a smooth tire sliding on a rough pavement surface. Kluppel's concept evaluates the hysteretic frictional force on a rubber cylinder sliding on a contact surface normal to the axis of the cylinder, by computing the energy dissipated in the

rubber due to the average stochastic excitation of the contact. Kluppel [11] adopted the view of Persson's theory of friction [12] and extended it by incorporating surface texture characteristics. In this method, the average stochastic excitation depth depends on the pavement surface properties, rubber properties, contact properties, sliding relative velocity and contact pressure. Therefore, first it is important to consider each of the above aspects separately.
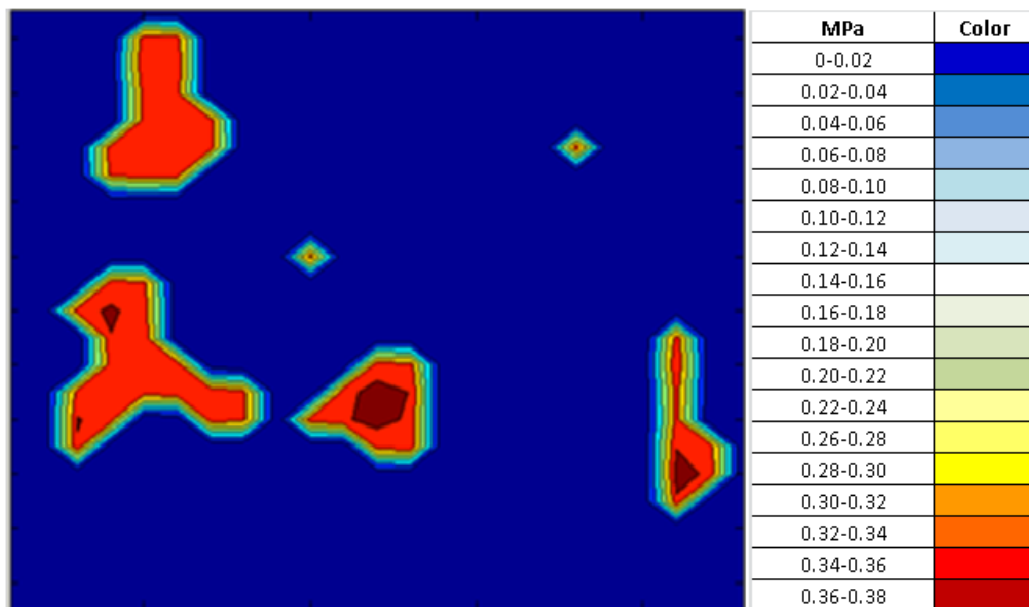
Figure 2.6: Contact patch pressure distribution from the numerical solution

2.3.1 Theoretical representation of pavement surface properties

In this section authors attempt to implement Kluppel's method to evaluate friction of a sliding tire on a random rough pavement. In the Kluppel's method the pavement surface parameters are estimated by assuming the geometric surface properties to be statistically stationary along the sliding distance. In previous work [13], it has been found that pavement surfaces generally have self- affine (fractal) characteristics. The self-affine surfaces have some similar characteristics for different length scales (e.g. micro scale and

macro scale). As an example, the local fractal dimension D of a self-affine surface which

is a quantitative measure of surface irregularity is same for both micro and macro scale

surface roughness. A higher variation in height profile (z(x)) gives higher D values. Apart

from the fractal dimension, two other properties are necessary to characterize a self-affine

surface. They are the correlation length $\xi_\parallel$ parallel to the surface and the variance, i.e., the

root mean square fluctuations around the mean height given by Equation 2.22;

$$\tilde{\sigma}^2 = \langle (z(x) - \langle z \rangle)^2 \rangle \tag{2.22}$$

where, $\langle z \rangle$ is the mean height of the surface points over the x-y domain considered in the

analysis. The variance $\tilde{\sigma}$ can also be expressed by the correlation length $\xi_\perp$ normal to the

surface as given in Equation 2.23;

$$\tilde{\sigma}^2 = \frac{1}{2}\xi_\perp^2 \tag{2.23}$$

The estimation of surface descriptors, i.e., the surface fractal dimension D and the

correlation lengths $\xi_\parallel$ and $\xi_\perp$, can be performed by evaluating the height-difference

correlation (HDC) function defined as;

$$C_z = \langle (z(x - \lambda) - z(x))^2 \rangle \tag{2.24}$$

where, z(x) and z(x + λ) are the surface heights at locations x and x + λ respectively. The

HDC is a measure of how strongly the neighboring points are related to each other. The

square values are averaged using the average ($\langle \ \rangle$) over all realizations of the rough

surface. Figure 2.7 shows a segment of the CT meter profile data observed at the test site

which was used to obtain the z(x) distribution.
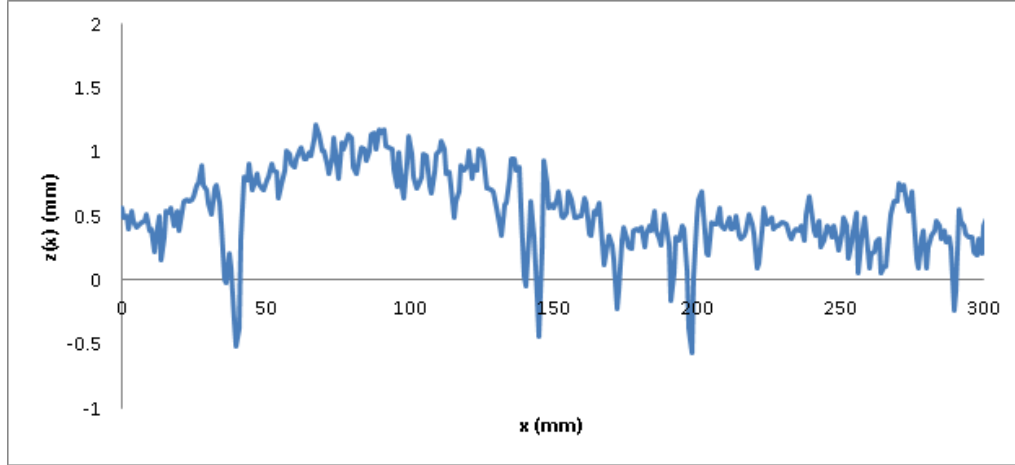
Figure 2.7: CT meter profile data observed at the test site

In the corresponding HDC plot (Figure 2.7) of $log(Cz(\lambda))$ vs $log(\lambda)$, $Cz(\lambda)$ increases with λ up to a particular value and then remains constant. From this it is clear that the neighbouring points on the surface have a higher correlation than the points that are distant from each other after which $Cz(\lambda)$ value does not change. The limiting λ is identified as $\xi_\parallel$. Therefore, the length dimensions higher than $\xi_\parallel$ do not affect the excitation of sliding. Similarly, $\xi_\perp$ can also be estimated based on the plot as follows. When a surface has higher variation of $Cz(\lambda)$ or a steep slope of the plot, the surface is identified as more irregular, i.e., the surface has a higher local fractal dimension D. Thus $\xi_\perp$ can be identified as the cut-off λ where the λ values greater than $\xi_\perp$ have no effect on excitation of rubber.

2.3.2 Characterization of the tire hysteretic friction

Rubber is assumed to be a viscoelastic material as discussed in Section 2.2.2. On the other hand, hysteretic friction is related to the energy dissipation in a viscoelastic media which can be written as,
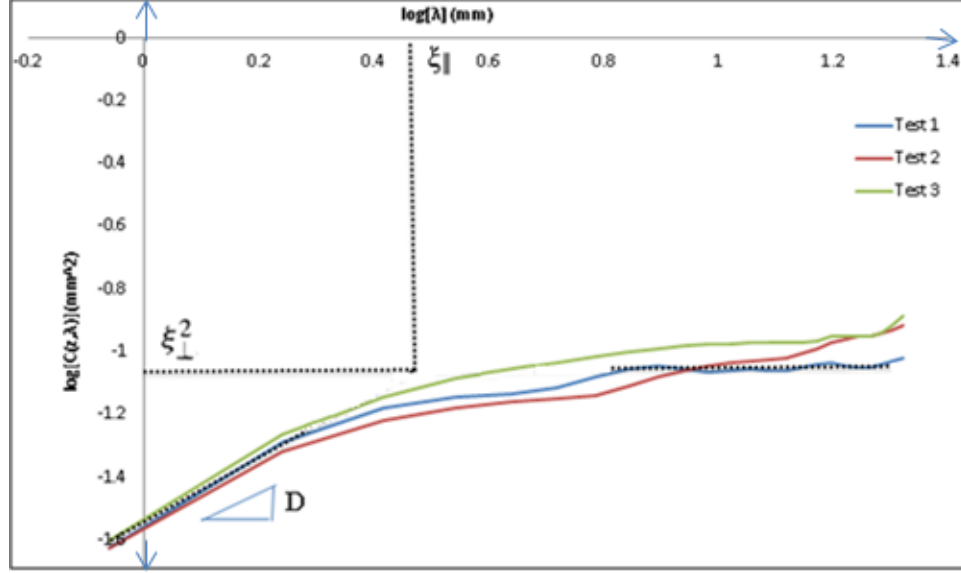
Figure 2.8: Height difference correlation (HDC) of the tested site

$$\Delta \tilde{E}_{diss} = \int_0^V \int_0^T \sigma . \dot{\varepsilon} \, d^3x \, dt \tag{2.25}$$

where, T is the excitation duration, $V = \int d^3 x$ is the excited volume of the rubber and σ and ε are the uniaxial stress and strain respectively. Energy dissipation can be computed in the frequency domain relatively easily by introducing the Fourier transforms of the stresses and strains shown in Equation 2.26 and Equation 2.27,

$$\sigma(t) = \frac{1}{2\pi} \int \hat{\sigma}(\omega) e^{-i\omega t} d\omega \tag{2.26}$$

$$\varepsilon(t) = \frac{1}{2\pi} \int \hat{\varepsilon}^*(\omega) e^{-i\omega t} d\omega \tag{2.27}$$

where, ω is the angular frequency of excitation of tire rubber by the pavement texture and $\hat{\varepsilon}^*$ is the delay of the response of strain compared to the stress in the time domain. Using the Fourier representation of Dirac delta function, the energy dissipation in Equation 2.28 can be expressed in terms of $E(\omega)$ the complex modulus of rubber which is a combination of loss and storage moduli, expressed as,

$$E(\omega) = E'(\omega) + iE''(\omega) = \frac{\hat{\sigma}(\omega)}{\hat{\varepsilon}(\omega)} \tag{2.28}$$

By assuming the surface profile $z(x)$ variation to be a stochastic process (random process), where the heights are proportional to the local strain of the rubber, the average energy ($\langle \quad \rangle$) dissipation over the domain can be expressed in terms of $S(\omega)$, the power spectral density of the rough surface. Finally, the hysteretic coefficient of friction can be obtained [14] as,

$$\mu_H = \frac{1}{4(2\pi)^3} \frac{\langle z_p \rangle (\beta - 1) \xi_\perp^2}{\sigma_0 \xi_\parallel v^2} \int_{\omega_{min}}^{\omega_{max}} \omega \left(\frac{\omega}{\omega_{min}} \right)^{-\beta} E''(\omega) \tag{2.29}$$

where, $\langle z_p \rangle$ is the mean penetration depth of the rubber into the surface, v is the relative sliding velocity, σ_0 is the apparent normal stress and $\beta = 7 - 2D$. Here, ω_{min} and ω_{max} can be determined by λ_{max} and λ_{min} respectively while $E''(\omega)$ can be determined by performing a dynamic modulus test for tire rubber.

2.3.3 Determination of contact properties

In Equation 2.29, the only unknown parameter is the average penetration depth $\langle z_p \rangle$ which has to be evaluated using the elastic contact properties. The elastic contact between rubber and rough surfaces typically occur at the summits of the highest asperities. A typical profile distribution with the distribution of summits is in Figure 2.8 where d is the distance between the two surfaces and $\phi_s(z)$ is the normalized distribution function of the surface summits which is assumed to be equal to the normalized distribution function $\phi(z)$ of the profile. The subscript s denotes the summits. The darkened area under the distribution function in Figure 2.8 is the probability that a summit is in contact with the rubber where ϑ_s is the variance of the summit height distribution. Figure 2.8 also shows that the deformations caused by the largest asperities can be assumed to be independent of the smallest asperities in contact. It is also clear that

the penetration depth depends on the shape of large aggregates defined by the surface curvature or amplitude. Greenwoods and Williamson (11) developed a rough surface contact theory (GW theory) where the relationship between the macrotexture surface geometric characteristics and surface contact characteristics were considered. This can be used to evaluate the average penetration depth $\langle z_p \rangle$ of the rubber into the asperities. This theory considers the variation of surface height along the sliding direction (m_0 parameter), square mean slope of surface height along the sliding direction (m_2 parameter) and the curvature of surface height along the sliding direction (m_4 parameter) as expressed in Equations 2.30, 2.31 and 2.32 respectively.

$$m_0 = \langle (z(x) - \langle z(x) \rangle)^2 \rangle \tag{2.30}$$

$$m_2 = \langle \left(\frac{dz}{dx} \right)^2 \rangle \tag{2.31}$$

$$m_4 = \langle \left(\frac{d^2z}{d^2x} \right)^2 \rangle \tag{2.32}$$

Greenwoods and Williamson defined a parameter α ($\alpha = m_0 m_4 / m_2^2$) which determines the variance of the surface summit distribution and the asperity density of the surface. It has been shown in the literature [12] that the parameter α determines the variance of surface summit distribution as;

$$\vartheta_s^2 = \left(1 - \frac{0.8968}{\alpha} \right) m_0 \tag{2.33}$$

The above analysis was extended to determine the rubber external area of contact A_c from the variance of surface summit distribution as;

$$A_c \approx \frac{(2D-4)A_0}{12\sqrt{3}(2D-2)} F_0 \left(\frac{d}{\vartheta_s} \right) \tag{2.34}$$

$F_0\left(\frac{d}{\vartheta_s}\right)$,the probability that asperity summits are in contact with rubber, is as

given by Equation 2.35 and A_o is the macroscopic surface area.

$$F_0\left(\frac{d}{\vartheta_s}\right) = \int_{\frac{d}{\vartheta_s}}^{\infty} \phi_s(z)\, dz \tag{2.35}$$

The GW theory can be expressed by the normalized distribution function $\phi(z)$ of

the surface $z(x)$, and the surface height variance $\bar{\sigma}^2$ and the mean distance d,

$$F_1\left(\frac{d}{\vartheta_s}\right) = \int_{\frac{d}{\vartheta_s}}^{\infty}\left(z - \frac{d}{\vartheta_s}\right)\phi(z)dz \tag{2.36}$$

Equation 2.36 is derived based on the relationship between the mean penetration

depth $\langle z_p \rangle$ and the normal stress which can be expressed in terms of $\langle z_p \rangle$ and the standard

deviation of the surface height as expressed in Equation 2.37.

$$\langle z_p \rangle = \tilde{\sigma} F_1\left(\frac{d}{\vartheta_s}\right) \tag{2.37}$$

This procedure was used to determine the $\langle z_p \rangle$ value in Equation 2.29 and the

analysis was performed as described in the following section.

2.3.4 Application of Kluppel's concept to a tire contact patch

In order to apply the Kluppel's method [15] which was developed for a cylindrical

contact surface for a tire patch, the tire patch has to be divided into sufficiently fine

rectangular contact elements which meet the requirements of the Kluppel's theory, i.e.

the length of a rectangle is at least six times higher than $\lambda_{\min}$. Generally the actual tire

contact shape changes with the applied vertical load, the tire pressure and several other

factors such as tire geometric cross-sectional and material properties as well as pavement

texture properties. However, for a given vertical load and tire pressure, the nominal

contact patch area can be estimated by the equivalent rectangular patch dimensions.

Therefore, the equivalent rectangular patch dimensions were used to define the tire patch area domain, which is subdivided into finer rectangular contact areas. The maximum dimension of the rectangular contact element was adjusted in order to be the same as $\xi_\parallel$ (Figure 2.8). Then the Kluppel's concept was applied locally at each rectangular contact patch element.

However, the local contact pressure (σ_0) at each contact patch element is a random quantity, which cannot be determined easily. In order to evaluate the contact pressures approximately the authors generated a random vertical deformation matrix with statistical properties similar to the asperity height distribution in the contact patch domain. Then the vertical pressure matrix was set up so that at each location the vertical deformation is proportional to the pressure. The proportionality constant was found by equating the vertical tire load and the resultant force of the entire contact patch.

2.3.5 Determination of the contact pressure distribution

The contact pressure distribution of a tire on a randomly rough surface depends on the properties of tire-pavement contact, the loading condition and the sliding speed. Hence, the local contact pressure at each contact patch element at each stage of motion is quite tedious to be determined. Therefore, it was also a difficult task to assign an appropriate contact pressure distribution when computing the hysteresis friction using the Kluppel's method. A modification was made to account for the fact that only the aggregate summits make contact with the tire. Since the contact patch is divided into fine rectangular elements, Kluppel's method can be applied at each element and the d value for each element can be estimated. The contact detection is satisfied when the d value corresponding to a particular location is smaller than the local summit height. Therefore,

at each segment of the contact patch, this criterion was used to define the contact. The penetration depth (z_p) at each point of contact can be evaluated by subtracting the summit by the average depth of penetration. In order to distribute the pressure at each point of contact to the neighboring points of contact, the pressure values were averaged. The resulting averaged pressure distribution in the contact surface is seen in Figure 2.9. The above analysis was repeated for several randomly generated profiles with the same statistical properties and the average values of the corresponding pressure profiles were determined.
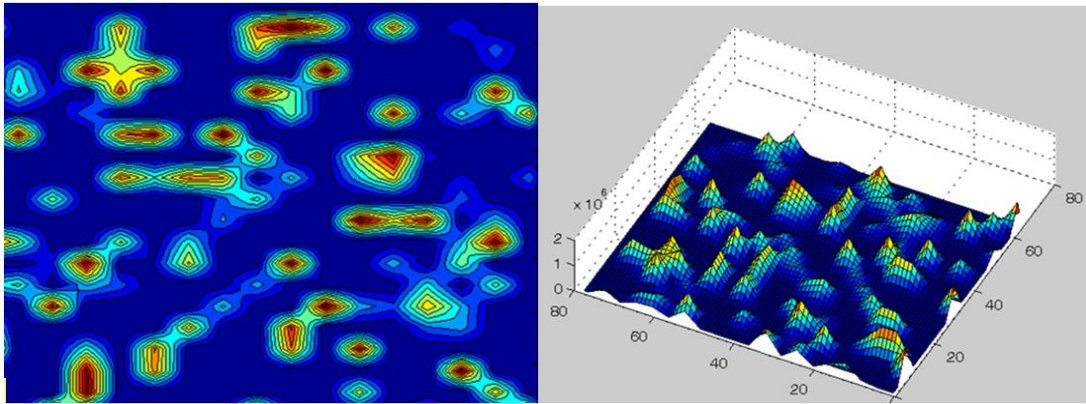
Figure 2.9: Pressure distribution under the tire (a) the contour map (b) 3D view

2.3.6 Comparison of the analytical model results with field test results

By repeating the analysis described in the previous section for different speeds and vertical loads, the corresponding coefficients of friction were evaluated using Equation 2.29. The comparison of the analytical predictions with the field test results is shown in Figure 2.10.

It is seen from Figure 2.10 that, as in the case of FE predictions, the analytical predictions of coefficient of friction are higher than the corresponding field values. This observation tends to further support the second explanation offered in Section 2.2.5.1 that

the moisture levels on the tested pavement to be in excess of what is just required to prevent the development of adhesion.
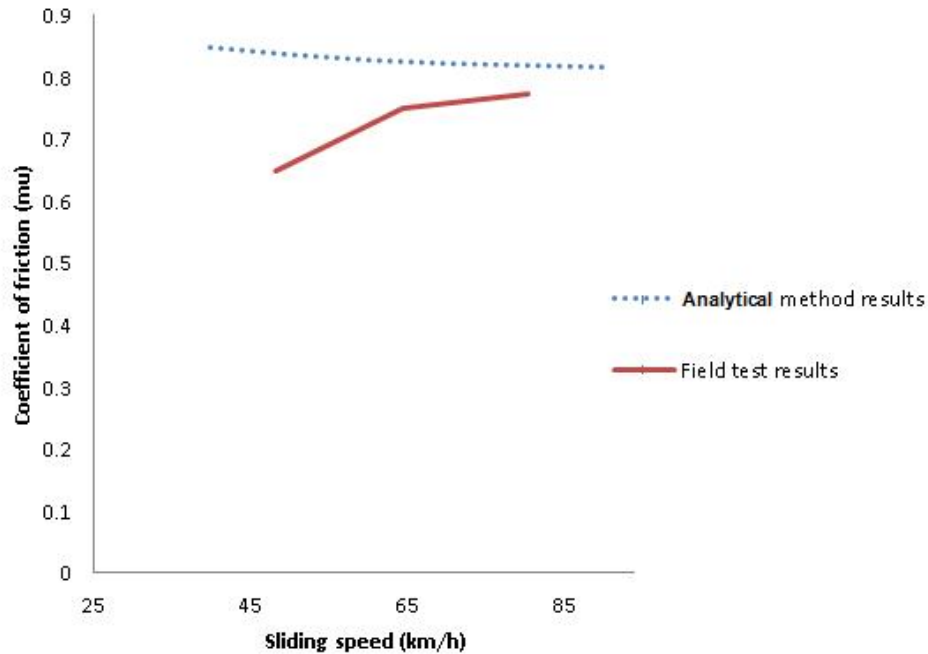
Figure 2.10: Comparison of analytical model predictions with field test results

Moreover, the analytical predictions show that the coefficient of friction decreases with increasing speed as opposed to the trend exhibited by the field results. This can be explained by the reduction in the loss modulus ($E^{//}$) of tire rubber in the range of indentation frequencies of the tire by the pavement macrotexture (Figure 2.11).When the tire sliding speed increases the frequencies of excitation of the tire by the pavement asperities increase as well. Therefore, the loss modulus and the hysteretic energy dissipation decrease with increasing speed consequently decreasing the coefficient of friction as well. However, it must be noted that the effects of tire heating on the loss modulus [16] which is significant in field testing and could explain the field observed trend, were not incorporated in the analytical model.
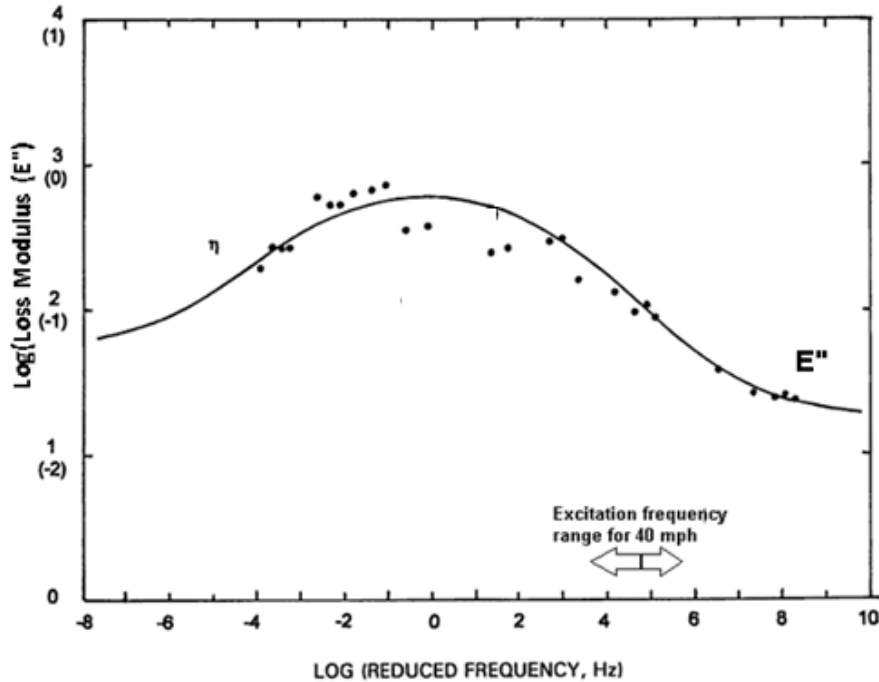
Figure 2.11: Loss modulus $E^{//}$ vs. frequency plot for SBR

2.4 Application of the results of the study

A major issue facing the runway and highway friction management community is the significant disparity of coefficients of friction values measured by different measuring devices on the same pavement surface. Therefore, there is an imminent need to harmonize friction measuring devices. For that purpose, numerical and analytical models such as the ones investigated in this study can be invaluable. Once any given friction measuring device is modeled numerically, parametric studies can be performed to explore the impacts of each significant tributary parameter such as the tire inflation pressure or the vertical load used in that device on its friction measurements. Then these parametric studies would provide a logical basis to adjust the tributary parameters of that device to harmonize its measurements with corresponding measurements of a standard device.

Such an exercise is practically impossible to be executed using field experimentation due to the excessive number of trials needed.

Furthermore, the analytical method in particular, when appropriately verified, can be used to evaluate real-time coefficients of friction experienced by a braking vehicle, if pavement texture can be measured in real-time and used as an input.

Moreover, both models evaluated in the study can be used as tools to design of asphalt concrete or cement concrete surfaces that optimize pavement friction. For this exercise, first the MPD values can be evaluated based on the aggregate gradation, air void content and bitumen content. Then the MPD values for different mixes can be used to randomly generate the corresponding pavement surfaces as an input to the analytical tools described in this study. Once the corresponding coefficients of friction are predicted, the optimum asphalt concrete mix which would provide the desired coefficient of friction can be determined without resorting to time consuming field trials. However, once a few promising mixes are identified, limited number of field trials can be performed using LWS tests for verification of the available skid-resistance.

2.5 Conclusion

The potential use of a finite element (FE) model and an analytical model that have the capability of predicting friction on a moist pavement based on pavement and tire properties was investigated. Predictions of both models on a selected asphalt concrete test surface matched reasonably well with each other although they exhibited opposite trends with increasing speed.

Hysteresis friction values predicted by both models were slightly higher than the corresponding field measurements which could be explained by the inability to regulate the field moisture level to be at the optimum needed to eliminate adhesional friction.

The FE model predictions showed a slight increasing trend with the travel speed as in the corresponding field measurements. However, the analytical predictions show a slight decreasing trend in the coefficient of friction with increasing speed. This can be directly attributed to the reduction of the loss modulus of SBR tire with increasing indentation frequency at the temperature considered in the simulation. The effects of tire heating which is significant in field testing were not incorporated in either of the model. Each prediction method can be improved in different ways. In the case of the FE method, the pavement texture can be modelled with a finer FE mesh without having to simplify the texture geometry at the asperity tips. On the other hand the analytical model can be improved by incorporating the temperature effects in the tire properties such as the loss modulus.

Field tests are impractical to evaluate friction in every critical condition because of the time and labor requirements encountered in setting up LWS tests. On the other hand, both friction prediction tools considered in this study can be used to simulate any desired field condition and finally verify a selected number of critical conditions with limited field testing. The analytical method is easily implemented on a computational basis compared to the FE method. Therefore, the analytical method in particular holds a lot of promise as a predictive tool of tire/pavement friction.

CHAPTER 3

NUMERICAL PREDICTION OF TRACTIVE FORCES ON A SMOOTH TIRE
SLIDING ON A RANDOMLY ROUGH WET PAVEMENT

3.1 Introduction

During rainy weather conditions automobiles and aircrafts could encounter significant reduction of steering and braking abilities due to reduction of tractive forces produced by the development of a water film between the tire and pavement surface. In general, factors affecting wet traction on a tire sliding on a random rough pavement can be categorized based on their sources of origin. Table 3.1 summarizes these factors. Due to the complex nature of the factors, the numerical simulation of tractive forces on a tire has always been a challenging task.

Table 3.1: Factors affecting wet traction

Domain	Factor
Tire	Carcass properties
	Inflation pressure
	Tread properties (not for smooth tires)
Pavement	Surface Texture (Macrotexture and Microtexture)
	Wearing characteristics
	Porosity
Water	Density
	Viscosity
	Water film depth
Operating conditions	Load
	Velocity
	Percent slip

3.2 Simulation of tractive forces on a smooth locked wheel sliding on a randomly rough pavement

The author made an attempt to numerically simulate the tractive forces on a smooth wheel sliding on a randomly rough pavement. Based on the characteristics of each domain, the simulation model was divided into two domains; fluid and tire domains. Simulation of the fluid domain involves modeling of water by considering principles of mass, momentum and energy conservation. This results in the Reynolds equation which has been simplified later by considering the dimensional factors and the conditions of analysis. The pavement roughness affects the water flow between the tire and the pavement. Therefore, pavement roughness conditions were also considered in the fluid flow simulation. Due to the flexible nature of the tire, deformations occur as a result of water pressure built against the tire surface. Hence the analysis results of the fluid model must be an input to the analysis of the tire model and vice-versa. This situation has been identified as the Fluid-Structure Interaction (FSI). This FSI analysis is repeated in the combined model until the deformation of the fluid and tire become compatible at the interface.

A MATLAB code was developed using the Finite Difference Method (FDM) for the fluid flow and tire models including FSI conditions in order to determine the tractive forces of a sliding tire on a randomly rough pavement. The major objective of developing the numerical model was to predict the wet friction forces. Subsequent efforts were made to determine the validity of the developed model and perform relevant parametric studies. Finally, the author also attempted to evaluate the feasibility of determining the viscous hydroplaning speeds under certain conditions, using the developed model.

3.3 Development of the numerical model

As indicated in Figure 3.1, as the tire slides on the pavement the entire tire patch loses contact with the pavement since the hydrodynamic pressure developed in front of the tire is adequate to inject enough water to occupy the interface. In a stationary observer frame of reference, the tractive force can be simulated by a wheel sliding along a wet pavement surface. In a moving wheel frame of reference on the other hand, the problem can be modeled as a layer of water on the pavement surface moving at a corresponding speed toward the wheel. In either case, a locked wheel is modeled in a sliding maneuver.

The development of the tire tractive force model is based on a simultaneous analysis of three aspects: (1) hydrodynamics of thin fluid films, (2) tire deformation characteristics and (3) uplift condition. The hydrodynamics of thin film fluid was analyzed in the fluid (water) flow model and the tire deformation characteristics were incorporated in the tire deformation model. Finally the uplift criterion of the tire was satisfied by balancing the tire load and the uplift load induced by the fluid film. As depicted in Figure 3.2, the contact patch was divided into a rectangular grid system and analyzed such that each node was made to satisfy the equilibrium criteria which will be discussed in this chapter.

3.3.1 Fluid flow model

The Reynolds equation (Equation 3.5) has been derived from the universal laws of conservation known as conservation of mass, conservation of momentum and conservation of energy. It enables the prediction of the fluid pressure distribution in the tire contact patch based on the tire and pavement geometry, boundary conditions and the

physical properties of water such as viscosity and density. The following assumptions are used to establish the Reynolds equation;
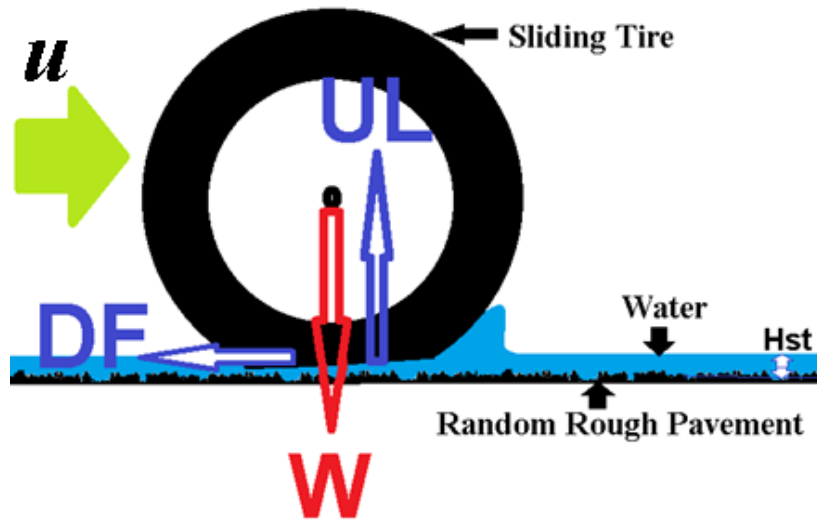

Figure 3.1: Forces acting on a tire sliding on a wet pavement
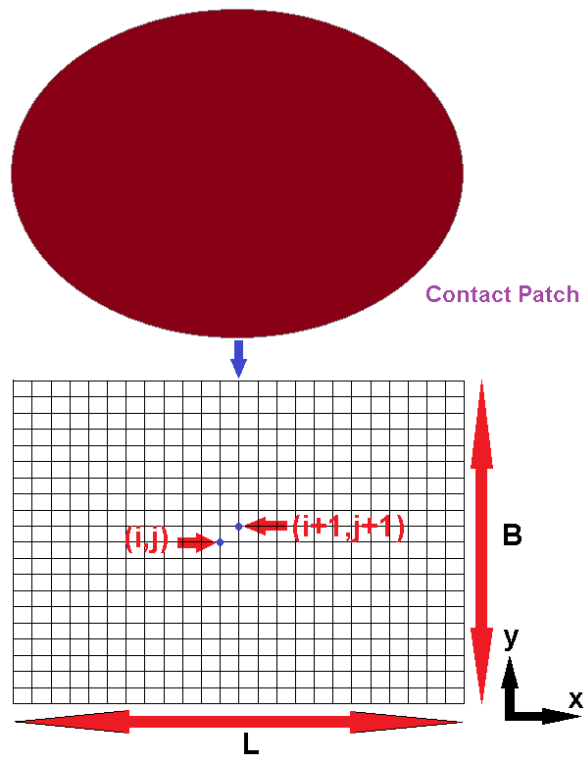

Figure 3.2: The rectangular grid domain in the tire contact patch

- Liquid is Newtonian

- Flow is laminar and independent of pressure

- Inertial force and gravity are neglected

- Lubricant is incompressible

- Viscosity is constant $(\eta = c)$

By considering an infinitesimally small moving fluid element the equation that results from the conservation of mass can be derived as seen in Equation 3.1, which is also known as the continuity equation in Cartesian notation. The symbols ρ, v, u, w and t represent the mean density, velocities in x, y and z directions and time respectively.

$$\frac{\partial \rho}{\partial t} + \frac{\partial \rho u}{\partial x} + \frac{\partial \rho v}{\partial y} + \frac{\partial \rho w}{\partial z} = 0 \tag{3.1}$$

The momentum equations are expressed in Equations 3.2 to 3.4. The forces considered include body forces f and the surface forces which include pressure p exerted on the surface by surrounding elements and the shear stresses exerted on the surface by fluid friction τ on the same fluid element.

$$\rho \frac{Du}{Dt} = -\frac{\partial p}{\partial x} + \frac{\partial \tau_{xx}}{\partial x} + \frac{\partial \tau_{yx}}{\partial y} + \frac{\partial \tau_{zx}}{\partial z} + \rho f_x \tag{3.2}$$

$$\frac{Dv}{Dt} = -\frac{\partial p}{\partial y} + \frac{\partial \tau_{xy}}{\partial x} + \frac{\partial \tau_{yy}}{\partial y} + \frac{\partial \tau_{zy}}{\partial z} + \rho f_{xy} \tag{3.3}$$

$$\rho \frac{Dw}{Dt} = -\frac{\partial p}{\partial z} + \frac{\partial \tau_{xz}}{\partial x} + \frac{\partial \tau_{yz}}{\partial y} + \frac{\partial \tau_{zz}}{\partial z} + \rho f_z \tag{3.4}$$

By applying the boundary conditions (i.e. no slip at the surfaces) and assuming the pressure to be independent of z due to the narrow gap between the two surfaces also by following several other steps [9] the equations of conservation of mass and

momentum can be combined and simplified to derive the Reynolds equations as shown in Equation 3.5.

$$\frac{\partial}{\partial x}\left(\frac{\rho h^3}{\eta}\frac{\partial p}{\partial x}\right) + \frac{\partial}{\partial y}\left(\frac{\rho h^3}{\eta}\frac{\partial p}{\partial y}\right) = 6u_s\frac{\partial(\rho h)}{\partial x} + 6\rho h\frac{\partial u_s}{\partial x} + 12\frac{\partial(\rho h)}{\partial t} \qquad (3.5)$$

3.3.1.1 Wedge effect

A wedge builds up in front of the tire thus increasing the film thickness in the direction of sliding. When water approaches the wedge, due to decreasing film thickness at the interface, pressure builds-up in the wedge area. The tire is subjected to a buildup of hydrodynamic pressure in the front due to the wedge effect thereby contributing to the separation of the tire from the pavement. Since this separation leads to reduced tractive forces the wedge term is very important in this study.

3.3.1.2 Squeeze effect

The squeeze term occurs in Equation 3.5 as a result of the pressure variation in the analysis domain. In this study, the atmospheric pressure acts on the tire boundary and inside the tire contact patch the pressure values are relatively higher. Therefore, a squeeze effect is generated within the tire and wet pavement contact patch under transient conditions.

3.3.1.3 Stretch effect

The stretch term in Equation 3.5 considers the rate at which the surface velocity changes in the sliding direction. This effect only occurs if the bodies in contact (tire and/or pavement) in the fluid boundaries are flexible and stretch the boundary surface along the direction of travel. They are neglected in this study since surface stretches are negligible in magnitude when compared to the radial deformations of the tire.

3.3.1.4 Non-dimensionalization of the Reynolds equation

Since the magnitude of the variables "pressure" in 10^6 Pa and "film thickness" in 10^{-6} m vary significantly, non-dimensionalization would be beneficial to solve the Reynolds equation faster by reducing the number of parameters. Therefore, non-dimensionalization was performed based on the Hertz's theory [24]. This theory has been derived based on the assumption of the geometry of the surfaces in the contact area locally can be accurately approximated by paraboloids because the film thickness and contact width are generally small compared to the local radius of the curvature of the bodies. In the current This theory provides the pressure profile, the geometry of the contact domain, and the elastic deformation of the contacting elements in the case of a loaded contact between two elastic bodies The Hertzian pressure profile is given by;

$$\left\{ p_h \sqrt{1 - \left(\frac{x}{a}\right)^2 - \left(\frac{y}{b}\right)^2} \; if \; |x^2 + y^2| < a^2 \atop 0 \right. \tag{3.6}$$

where, p_h refers to the maximum Hertzian pressure in the contact patch:

$$p_h = \frac{2.5F}{2\pi a^2} \tag{3.7}$$

where, F is the external load and a is the radius of the contact patch which is assumed to be circular in the Hertzian's derivations;

$$a^2 = \frac{2.5FR_x}{2E'} \tag{3.8}$$

where, R_x is the reduced radius of curvature of the two bodies in contact in the x direction ($R_x = R_y$ for a circular contact) and E' is the reduced elastic modulus of the contacting bodies. Here the reduced radius of curvature R is given by $\frac{1}{\frac{1}{R_1}+\frac{1}{R_2}}$, where R_1 and R_2 are the

radii of curvature of two contacting bodies. The reduced elastic modulus E' is given by $\frac{1}{\frac{1}{E_1}+\frac{1}{E_2}}$, where E_1 and E_2 are moduli of two contacting bodies. Since the pavement modulus value is infinitely large based on the rigid pavement assumption the reduced elastic modulus becomes equal to the tire material elastic modulus. The dimensionless Reynolds equation as given in Equation 3.9 can be obtained by converting all the variables in the Reynolds equation into dimensionless variables given below;

$$\frac{\partial}{\partial X}\left(\varepsilon\frac{\partial P}{\partial X}\right) + \frac{\partial}{\partial Y}\left(\varepsilon\frac{\partial P}{\partial Y}\right) - \frac{\partial(\bar{\rho}H)}{\partial X} - \frac{\partial(\bar{\rho}H)}{\partial T} = 0 \tag{3.9}$$

$$\begin{aligned}
\bar{\rho} &= \rho/\rho_0, \\
\bar{\eta} &= \eta/\eta_0, \\
X &= x/a, \\
Y &= y/a, \\
P &= p/p_h, \\
H &= hR/a^2, \\
T &= tu_s/(2a),
\end{aligned}$$

where, h is the fluid thickness and, ρ_0 and μ_0 are the density and the viscosity at the ambient pressure.

3.3.1.5 Discretization of the Reynolds equation

The nonlinear Reynolds equation has been discretized and solved to obtain the pressure distribution in the contact region. The spatial domain $X \in [X_L, X_R]$ is discretized with a uniform grid of $n+1$ points X_i $(0 \leq i \leq n)$ with mesh size h_x. Then the following finite difference approximations have been used in converting the Reynolds equation to the equivalent numerical form.

$$\frac{\partial}{\partial X}(\rho H)_{X_i} \approx \frac{(\rho H)_i - (\rho H)_{i-1}}{h_X} = \frac{\rho_i H_i - \rho_{i-1}H_{i-1}}{h_X}$$

$$\frac{\partial}{\partial X}(\varepsilon\frac{\partial P}{\partial X})_{X_i} \approx \frac{(\varepsilon\frac{\partial P}{\partial X})_{i+1/2} - (\varepsilon\frac{\partial P}{\partial X})_{i-1/2}}{h_X}$$

$$(\varepsilon\frac{\partial P}{\partial X})_{i+1/2} \approx \varepsilon_{i+1/2}(\frac{P_{i+1} - P_i}{h_X})$$

$$(\varepsilon\frac{\partial P}{\partial X})_{i-1/2} \approx \varepsilon_{i-1/2}(\frac{P_i - P_{i-1}}{h_X})$$

and, $\varepsilon = \frac{\rho H^3}{\eta\lambda}$ where, $\varepsilon_i = \frac{\rho_i H_i^3}{\eta_i\lambda}$ $\longrightarrow$ $\varepsilon_{i+1/2} = \frac{\varepsilon_i + \varepsilon_{i+1}}{2}$

$\longrightarrow$ $\varepsilon_{i-1/2} = \frac{\varepsilon_i + \varepsilon_{i-1}}{2}$

Similarly the spatial domain $Y \in [Y_L, Y_R]$ is discretized with a uniform grid of n +1 points Y_i ($0 \le i \le n$) with mesh size h_y and the time domain $T \in [0, T_f]$ is discretized using a time increment of ΔT. Then the discretized Reynolds equation (Equation 3.10) can be written as,

$$\frac{(\epsilon_{i-1,j}^n + \epsilon_{i,j}^n)(P_{i-1,j}^n - P_{i,j}^n) + (\epsilon_{i+1,j}^n + \epsilon_{i,j}^n)(P_{i+1,j}^n - P_{i,j}^n)}{2(\Delta X)^2}$$
$$+ \frac{(\epsilon_{i,j-1}^n + \epsilon_{i,j}^n)(P_{i,j-1}^n - P_{i,j}^n) + (\epsilon_{i,j+1}^n + \epsilon_{i,j}^n)(P_{i,j+1}^n - P_{i,j}^n)}{2(\Delta Y)^2}$$
$$- \frac{\rho_{i,j}^n H_{i,j}^n - \rho_{i-1,j}^n H_{i-1,j}^n}{\Delta X} - \frac{\rho_{i,j}^n H_{i,j}^n - \rho_{i,j}^{n-1} H_{i,j}^{n-1}}{\Delta T} = 0$$

(3.10)

where, $\Delta X = h_x$, $\Delta Y = h_x$ and the superscript n denotes values at time t_n. Based on the assumption of homogeneous density in the analysis domain, $\rho_{i,j}^n = \rho$. The equation to evaluate the height based on the tire deformation and pavement roughness is given in Equations 3.10 and 3.11 have been solved simultaneously. The solution procedure is discussed in Section 3.4.

$$h(x, y, z, t) = d(x, y, z, t) + \Delta h(x, y, z, t)$$

(3.11)

where, $h(x, y, z, t)$ = Depth of the water flow at the (x,y,z) point at time t=t, $d(x, y, z, t)$ = Pavement roughness height at the (x,y,z) point at time t=t and $\Delta h(x, y, z, t)$ = tire deformation at the (x,y,z) point at time t=t.

3.3.2 Tire model

As indicated in Figure 3.3, the smooth tire was modeled using a 3-dimensional spring model. The radial springs (with a spring coefficient k) over the x domain are spanned at distances of dx at the contact patch while the radial springs over the y domain are spanned at distances of dy at the contact patch. Each radial spring is connected to four adjoining radial springs by four interconnecting springs (of spring constant q). The spring coefficients of the radial and interconnecting springs are defined as functions of the tire inflation pressure. This model has been used in a previous research as a spring tire model by replacing the intermediate springs by interconnecting radial springs [25].
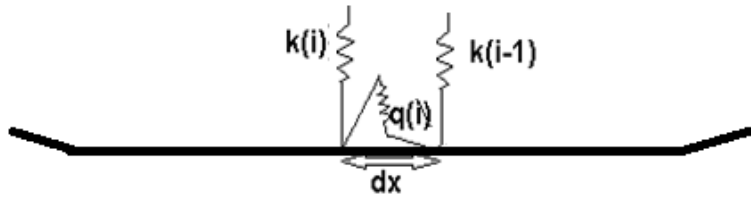

Figure 3.3: Spring diagram of the tire model

As indicated in Figure 3.4(a), the single point contact radial spring free body diagram and the displacement diagram shown in Figure 3.4(b) were used to estimate the radial displacement at the contact due to the water uplift force which can be derived from Equation 3.11.
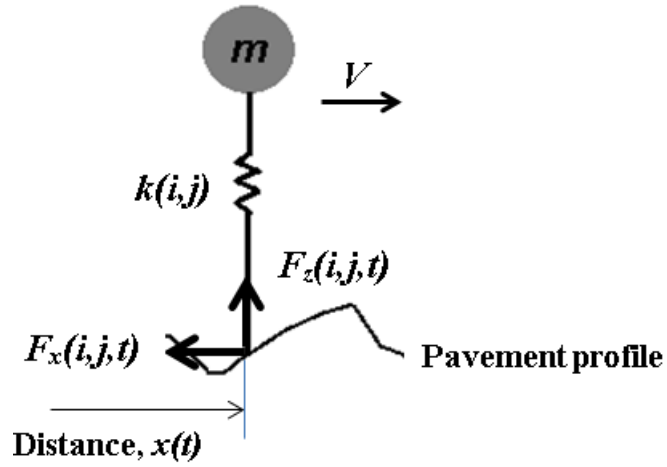
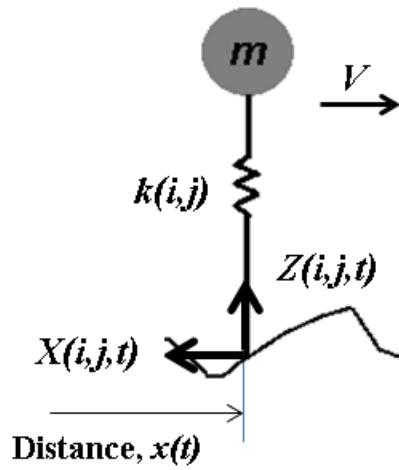Figure 3.4 (a): Free body diagram of a radial spring

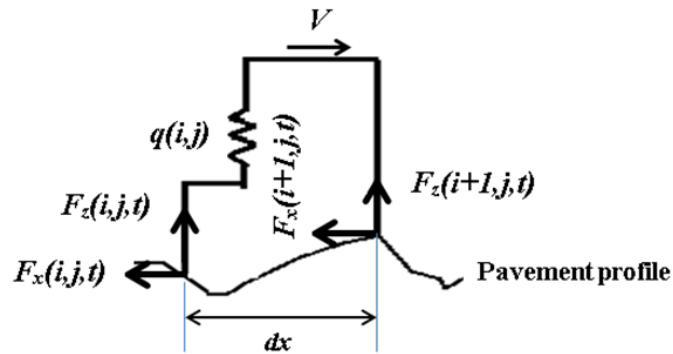Figure 3.4 (b): Displacement diagram of a radial spring

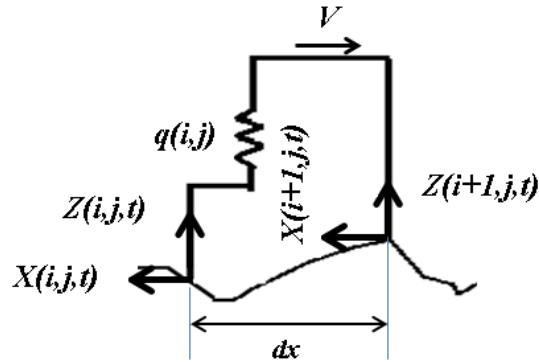Figure 3.4 (c): Free body diagram of an adjoining radial spring

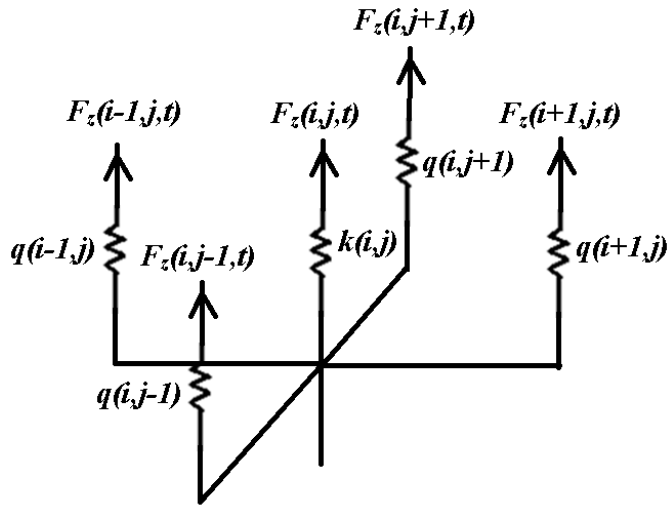Figure 3.4 (d): Displacement diagram of an adjoining radial spring

Figure 3.4 (e): Free body diagram of the combined radial and adjoining system
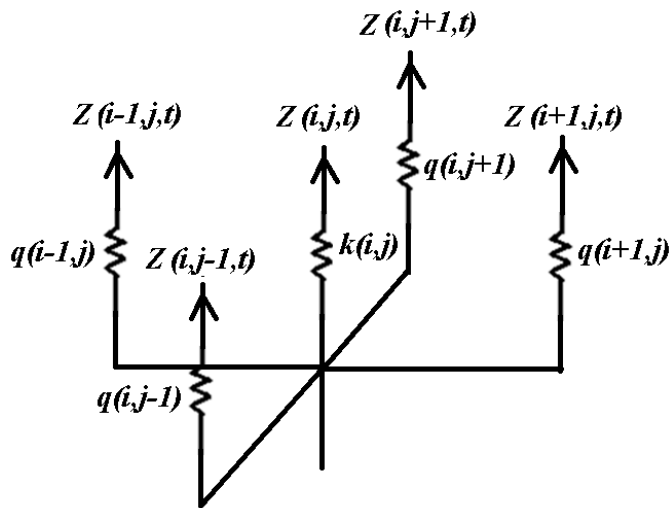

Figure 3.4 (f): Displacement diagram of the combined radial and adjoining system

$$F_z(i,j,t) = -k(i,j,t)*Z(i,j,t) \qquad (3.11)$$

75

where, $Fz(i,j,t)$ is the contact force in the z-direction at the point (i,j) when the time, $t=t$,

$Z(i,j,t)$ is the displacement in the z-direction at the point (i,j) when the time, $t=t$ and

$k(i,j,t)$ is the spring coefficient at the point (i,j) which can be derived from;

$$k(i,j,t) = (2.68*P_{inf}*(L*1000*B*1000)^{\wedge}(0.5)+33.1)*10000 \tag{3.12}$$

where, P_{inf} is the inflation pressure in MPa, L and B are length and width of the contact patch

in meters respectively. Similarly, by referring to Figure 3.4(c) and (d), the dual point contact

adjoining radial spring was used to estimate the vertical shear displacement at the contact due to

the water uplift force can be derived from Equation 3.13.

$$F_z(i,j,t)- F_z(i+1,j,t)= -q(i,j,t)*(Z(i,j,t)- Z(i+1,j,t)) \tag{3.13}$$

where, $q(i,j,t)$ is the spring coefficient of the adjoining spring which can be derived from

$$q(i,j,t)=(2.68*P_{inf}*(L*1000*B*1000)^{\wedge}(0.5)+33.1)*10000 \tag{3.14}$$

Similarly deriving the equations for all the springs in the spring system shown in

Figure 3.4(e) and (f);

$$F_z(i,j,t)- F_z(i-1,j,t)= -q(i,j,t)*(Z(i,j,t)- Z(i-1,j,t)) \tag{3.15}$$

$$F_z(i,j,t)- F_z(i,j+1,t)= -q(i,j,t)*(Z(i,j,t)- Z(i,j+1,t)) \tag{3.16}$$

$$F_z(i,j,t)- F_z(i,j-1,t)= -q(i,j,t)*(Z(i,j,t)- Z(i,j-1,t)) \tag{3.17}$$

and then by getting the summation of Equation 3.11, 3.13, 3.15, 3.16, 3.17;

$$\begin{aligned}
&F_z(i,j,t)+ F_z(i,j,t)- F_z(i+1,j,t)+ F_z(i,j,t)- F_z(i-1,j,t)+ F_z(i,j,t) - \\
&F_z(i,j+1,t)+ F_z(i,j,t)- F_z(i,j-1,t)= -k(i,j,t)*Z(i,j,t) -q(i,j,t)*(Z(i,j,t)- \\
&Z(i+1,j,t)) -q(i,j,t)*(Z(i,j,t)- Z(i-1,j,t)) -q(i,j,t)*(Z(i,j,t)- Z(i,j+1,t)) \\
&-q(i,j,t)*(Z(i,j,t)- Z(i,j-1,t))
\end{aligned} \tag{3.18}$$

By assuming the forces are uniform around the node between the radial springs

and adjoining springs (this assumption was made after performing the analysis with the

assumption and without the assumption. Both results did not show a difference since the results were averaged over the time domain. The analysis encountered convergence difficulties without this assumption);

$$Z(i,j,t+1)=1/(k(i,j,t)+4q(i,j,t))*(-F_z(i,j,t)+$$
$$q(i,j,t)*(Z(i-1,j,t)+Z(i+1,j,t)+Z(i,j+1,t)+Z(i,j-1,t)))$$
(3.19)

$$F_z(i,j,t)=-(k(i,j,t)+4q(i,j,t))*Z(i,j,t)-q(i,j,t)*(Z(i-1,j,t)$$
$$+Z(i+1,j,t)+Z(i,j+1,t)+Z(i,j-1,t))$$
(3.20)

Here $F_z(i,j,t)=ULF(i,j,t)+WF(i,j,t)$ where, $ULF(i,j,t)$ is the uplift force at the point (i,j) when time $t=t$, $WF(i,j,t)$ is the tire load at the point (i,j) when time $t=t$, Here $WF(i,j)$ is determined at each node by assuming a parabolic vertical tire load distribution in the contact patch under the tire. Therefore;

$$Z(i,j,t+1)=(1/(4q(i,j,t)-k(i,j,t)))*q(i,j,t)*(Z(i-1,j,t)-Z(i+1,j)+Z(i,j-$$
$$1,t)-Z(i,j+1,t))-(1/(4q(i,j,t)-k(i,j,t)))*((ULF(i,j,t)+WF(i,j,t));$$
(3.21)

3.4 Numerical solution procedure

A MATLAB program was developed to solve the discretized non-dimensional Reynolds equation and the tire model including the tire-water interaction. In the program, the initial values of length of the contact patch ($L=X_L$- X_R) was determined by performing an approximate preliminary analysis which satisfies the convergence criteria while the width ($B=Y_L$- Y_R) was assigned as 80 mm. This will be discussed later in this section. The boundary conditions are set such that all exterior boundaries have the atmospheric pressure.

3.4.1 Analysis of smooth pavement surfaces

3.4.1.1 The steady state solution

A preliminary closed form solution was observed for a rectangular plate with an infinite width and 100 mm long sliding on a flooded smooth surface which was tapered into the direction of sliding on a pavement with a standing water height of 1 mm. Then the results were compared with a similar numerical model developed in MATLAB. The results are depicted in Figure 3.5. Based on the Figure the MATLAB program results are fairly agreed with the closed form results.
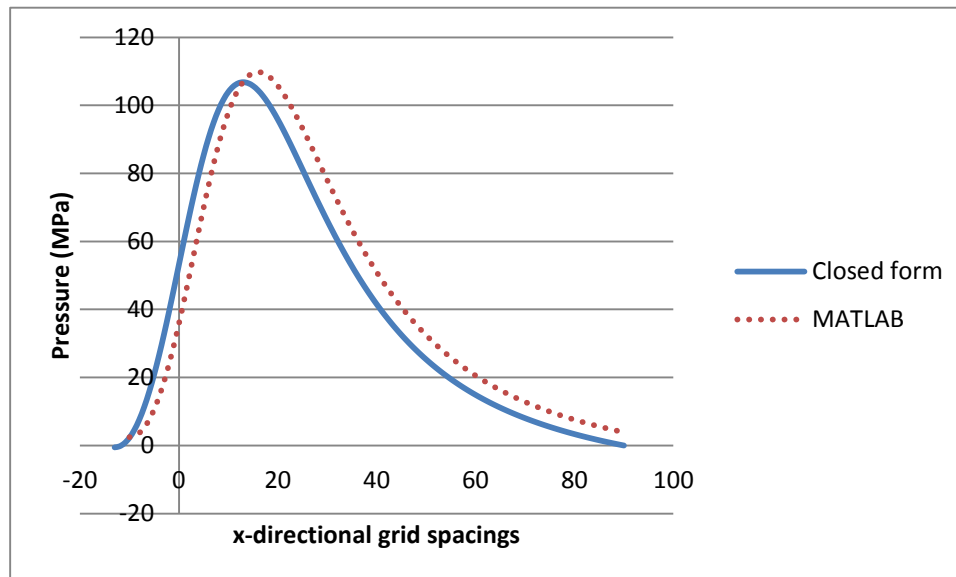

Figure 3.5: Comparison of the closed form solution and the MATLAB program

In the first phase, the analysis was performed only in the space domain by neglecting the time domain variations where the following "squeeze term" was neglected. The space domain (contact patch) was divided into 100 x 100 elements with the number of nodes in one direction being 101. The sliding speed (u) was considered as 65 mph (10 m/s). Analysis was performed iteratively until the uplift force induced on the tire surface due to the water pressure is approximately equal to the tire load. Figure 3.7 shows the

pressure plot from the analysis of phase 1 which clearly indicates higher pressure values in front of the tire with respect to the sliding direction. This peak clearly indicates the water approaching to the front of the tire subjects to the wedge effect and starts developing high pressure values as described in section 3.3.1.1.
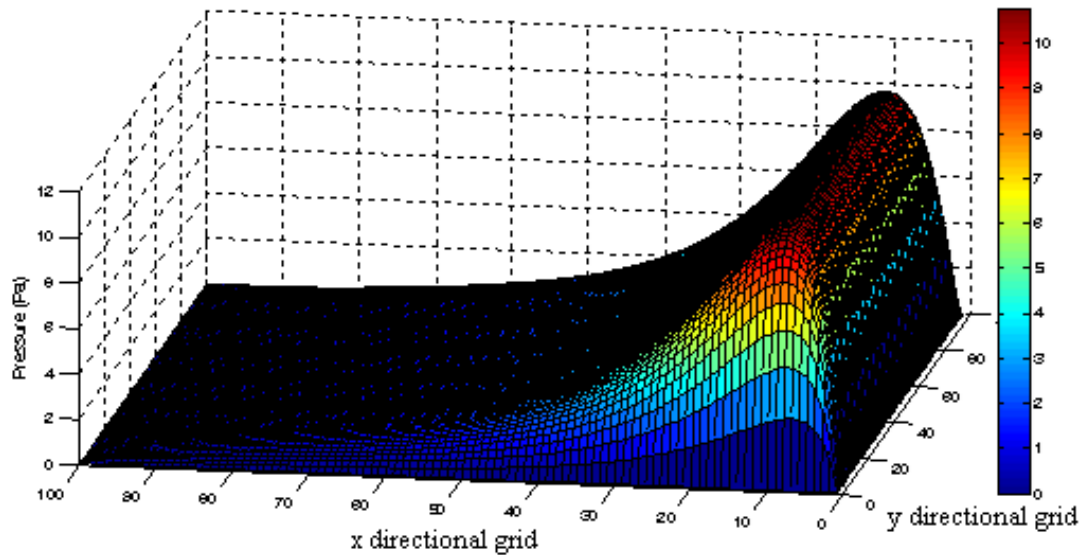

Figure 3.6: Pressure plot for the steady state analysis

3.4.1.2 The transient solution

Similarly, the second phase of the analysis was performed in both the space as well as the time domains. This was achieved by increasing the sliding speed with time in each analysis loop. In order to compare the transient solutions obtained for a given ultimate speed with the steady state solution for that speed, the sliding speed in the transient analysis was increased in steps and maintained constant at the desired steady state analysis performed (65 mph). Figure 3.7 shows the pressure plot of the transient analysis at a speed of 65 mph. Figure 3.8 shows both steady state and transient pressure along the sliding direction (*X*) plotted on the same plot. Since the transient analysis is more time consuming when compared with the steady state analysis, the convergence criteria of the transient analysis were relaxed than that of the steady state analysis. As it

can be seen in Figure 3.9, the difference between the two pressure plots could be explained by the higher tolerance allowed in the transient analysis.
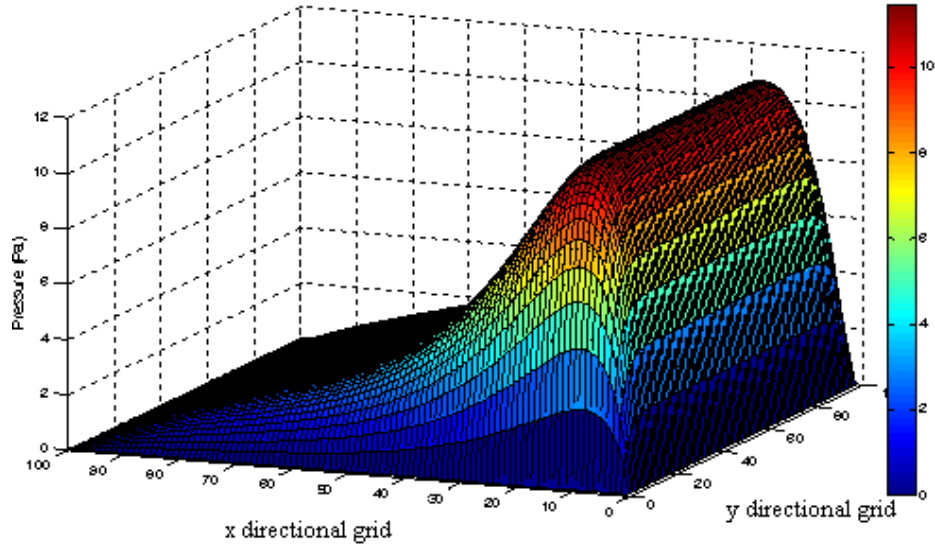

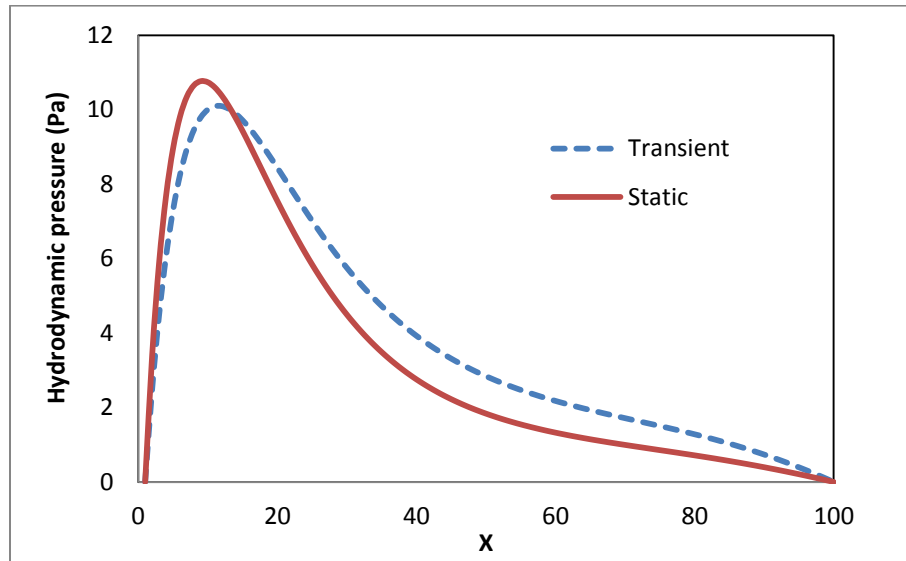Figure 3.7: Pressure plot for the transient analysis

Figure 3.8: 2D pressure plot comparison for steady state and transient analyses

3.4.2 Analysis of random rough pavement surface condition

Pavement roughness has been incorporated in the model by including a random variation into the water film thickness Equation. The results of field texture

measurements observed using a CT meter were converted to Mean Texture Depth (MTD) as described in Chapter 2. Then the MTD values have been used to generate a normally distributed random pavement profile in the MATLAB program. A random pavement profile has been generated at each iteration. Figure 3.10 shows the variation of uplift pressure of water acting on the tire surface at a particular instance (time step) in the analysis. Since the pavement surface has a random nature, the pressure plot also shows a random variation over the contact domain. However, the pressure spike built in the domain could be explained by the instability caused by the sudden pressure drop from a very high value to a very low value in the boundary. As depicted in Figure 3.9(a), (b) and (c), the tire patch was dragged to the sliding direction at a rate of one x directional grid spacing per one time step such that the size of the time step defined as $\varDelta t$ (sec)=(x directional grid spacing (m))/ (sliding speed (u(m/s))). The 3-dimensional pavement profile is shown in Figure 3.11. The analysis was continued for a number of time steps until all the convergence criteria are satisfied. Those convergence criteria are; (1) the force equilibrium where uplift force *(UL)* $>=$ tire load (*W*) and (2) the minimum film thickness *(h_{min})* > threshold value. Then the uplift pressure values were averaged. Since the program averages the results over a number of time steps and the pressure spike observed in Figure 3.11 decreases with time. The average pressure distribution is shown in Figure 3.12.
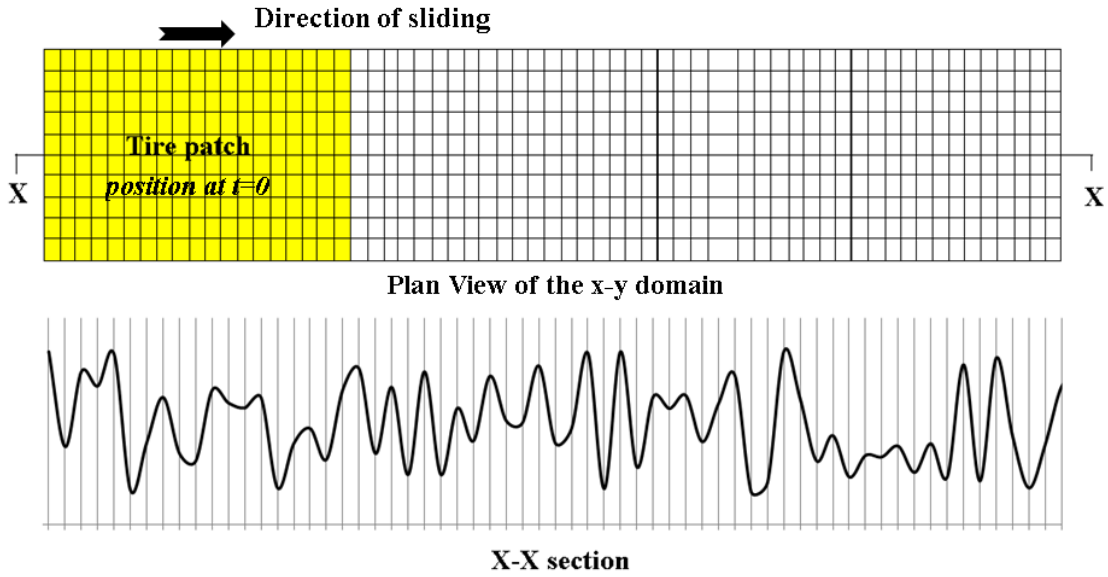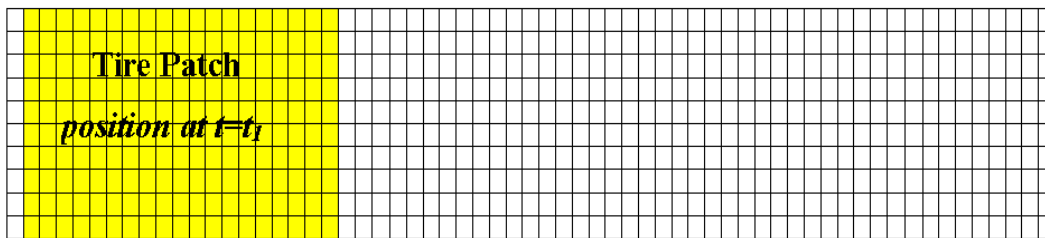
Figure 3.9 (a): The tire patch location at t=0

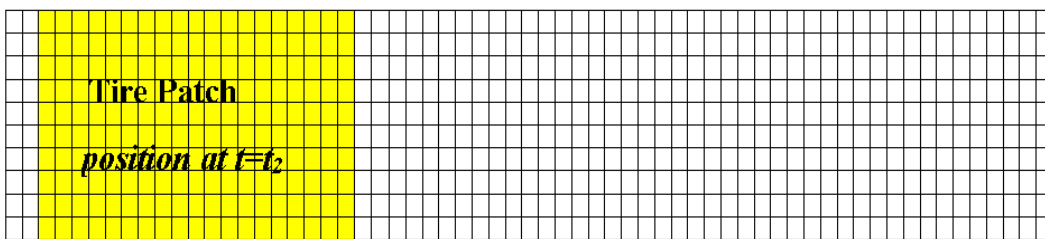Figure 3.9 (b): The tire patch location at t=t_1

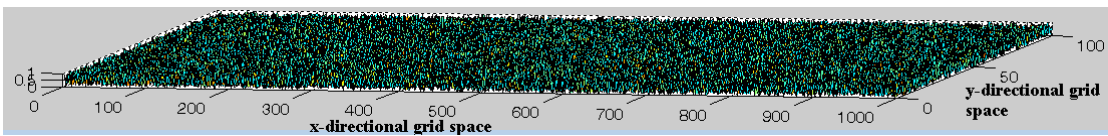Figure 3.9 (c): The tire patch location at t=t_2
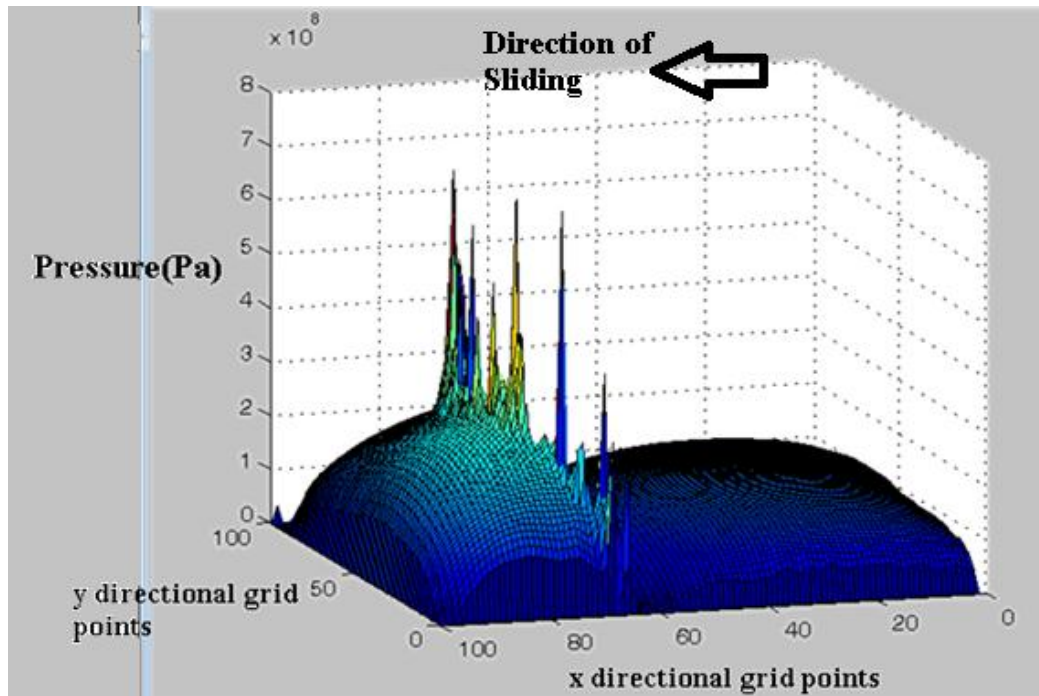

Figure 3.10: 3D randomly rough pavement

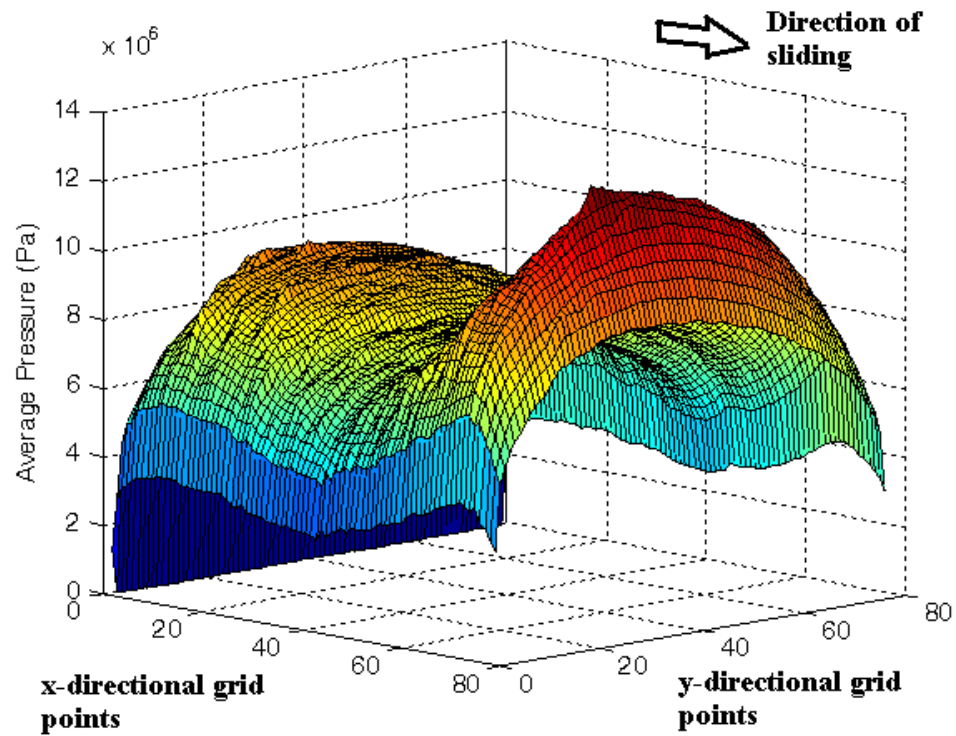Figure 3.11: Uplift pressure distribution in the contact domain

Figure 3.12: 3D average pressure plot

83

3.4.2.1 Determination of drag forces

Determination of the drag force is very important to evaluate in this study since when a sliding tire is completely separated from the pavement the drag force is the only force which helps in maneuvering the vehicle by providing the required friction. The study was continued by calculating the drag forces along the sliding direction (x direction) based on Equation 3.21.

$$F_{drag,x} = \frac{\eta u}{h} + \frac{h}{2}\frac{dP}{dx}$$ (3.21)

3.5 Sensitivity analysis of the numerical model

Sensitivity analysis is a technique used to determine how different values of input variables will impact the output under a given set of assumptions. The mesh size and the number of analysis steps were considered as input variables and the drag force is considered as the output variable. Each input variable was changed gradually while calculating the uplift forces and the results were plotted as shown in Figure 3.13(a) and (b) while keeping the following parameters constant at the indicated values;

- Tire inflation pressure – 25 psi

- Tire contact width – 80 mm

- Average roughness height – 0.1 mm

- Sliding speed – 30 mph

Based on the sensitivity analysis, it is seen that the drag force is not sensitive to the contact grid size for grid sizes greater than 100 and it is also not sensitive to the number of time steps when number of time steps are higher than 1500. Therefore, the ensuring parametric study was conducted with a grid size of 100 and 1500 time steps.
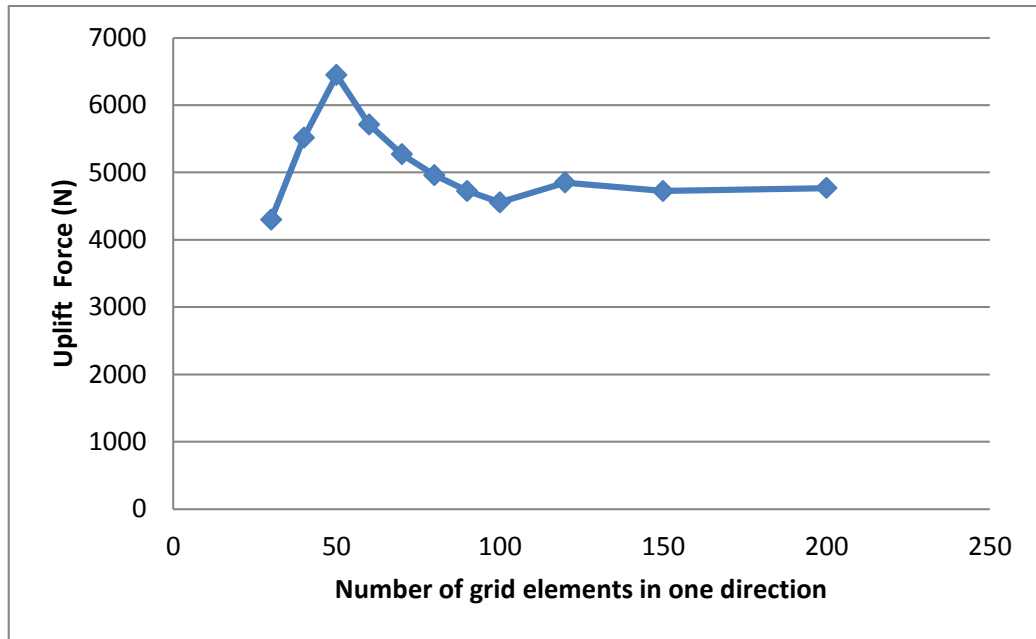
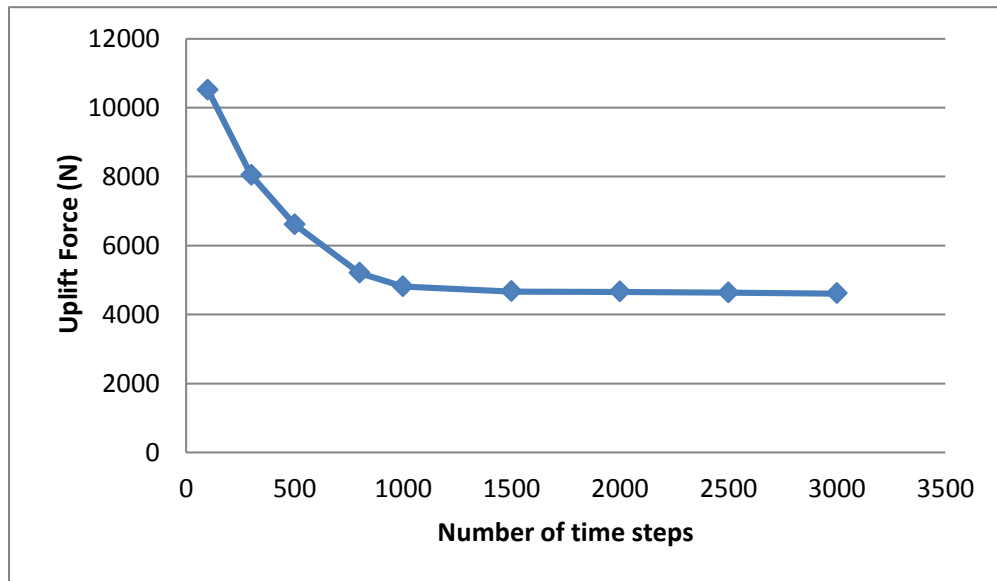Figure 3.13(a): Sensitivity analysis for the contact grid size

Figure 3.13(b): Sensitivity analysis for the number of time steps

3.6 Parametric study

A parametric study was conducted to evaluate the effect of several significant parameters on the drag force of a smooth tire sliding on a random rough surface. These

parameters were standing water film thickness, tire inflation pressure, sliding speed, average roughness height and tire width.

3.6.1 Effect of standing water film thickness on drag force

The standing water film thickness on the pavement was varied from 1 mm to 10.5 mm while keeping the following parameters constant at the indicated values;

- Tire inflation pressure – 25 psi

- Tire contact width – 80 mm

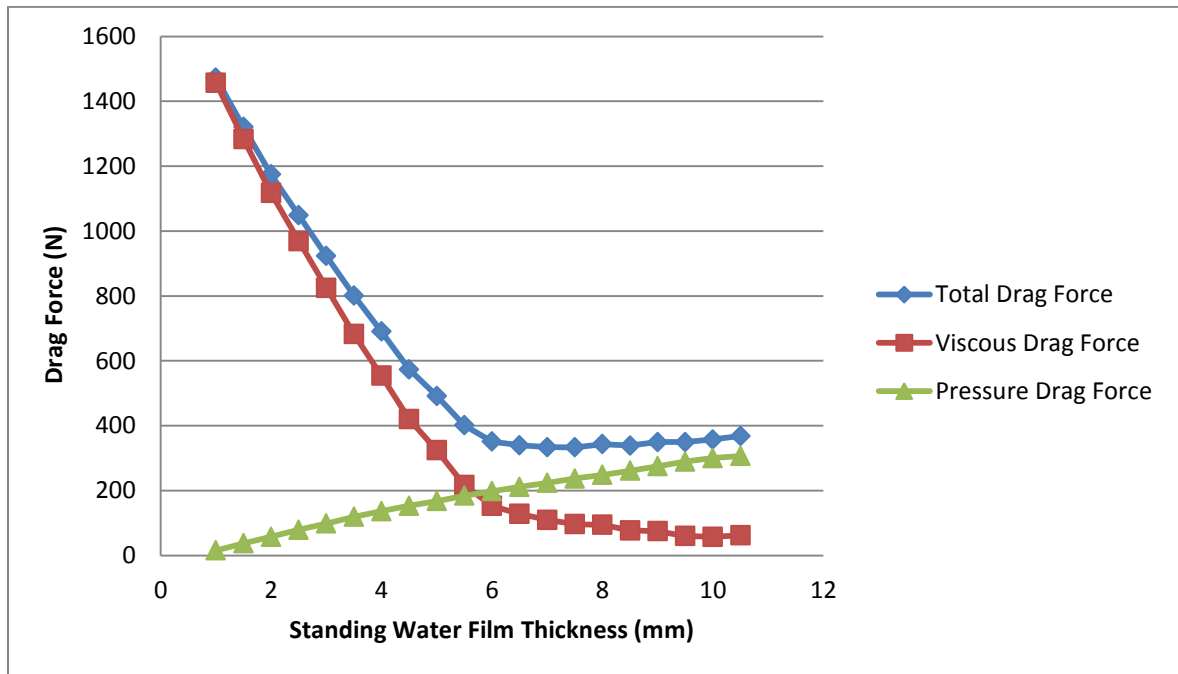- Average roughness height – 0.1 mm

- Sliding speed – 30 mph

Figure 3.14: Effect of standing water film thickness to drag force

Based on Figure 3.14 it can be seen that the total drag force (viscous drag + pressure drag) decreases with increasing standing water film thickness until 6mm and then increased. However when considering the viscous drag and pressure drag separately

in the plot, it is seen that the viscous drag decreases with increasing standing water film thickness while the pressure drag increases with increasing standing water film thickness. Therefore, the total drag force has the decreasing and increasing trends with a minimum at 6 mm of film thickness.

3.6.2 Effect of tire sliding speed on drag force

The sliding speed of the tire was varied from 30 mph to 60 mph while keeping the following parameters constant at the indicated values and the results are plotted in Figure 3.15;

- Tire inflation pressure – 25 psi

- Tire contact width – 80 mm

- Average roughness height – 0.1 mm

- Tire load – 4850 N
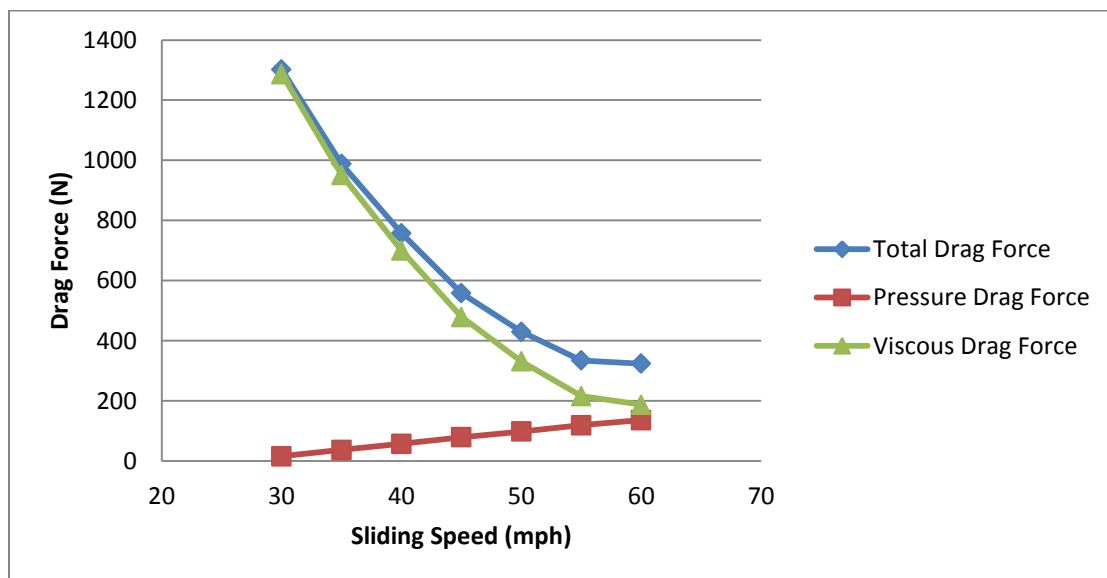
- Standing water film thickness – 1 mm

Figure 3.15: Effect of sliding speed to drag force

Based on Figure 3.15, it can be seen that the drag force decreases with increasing tire sliding speed. It is well known that higher sliding speeds reduce viscous drag forces in the contact region. Therefore, higher sliding speeds have lower drag force when the film thickness is low. However, when the film thickness is high and if there is sufficient amount of water in front of the tire, pressure will be built-up in front of the tire causing the increase in pressure drag, i.e. the total drag force.

3.6.3 Effect of inflation pressure to drag force

The tire inflation pressure was varied from 18 psi to 35 psi while keeping the following parameters constant at the indicated values and the results are plotted in Figure 3.16;

- Sliding speed – 45 mph

- Tire contact width – 80 mm

- Average roughness height – 0.1 mm

- Tire load – 4850 N

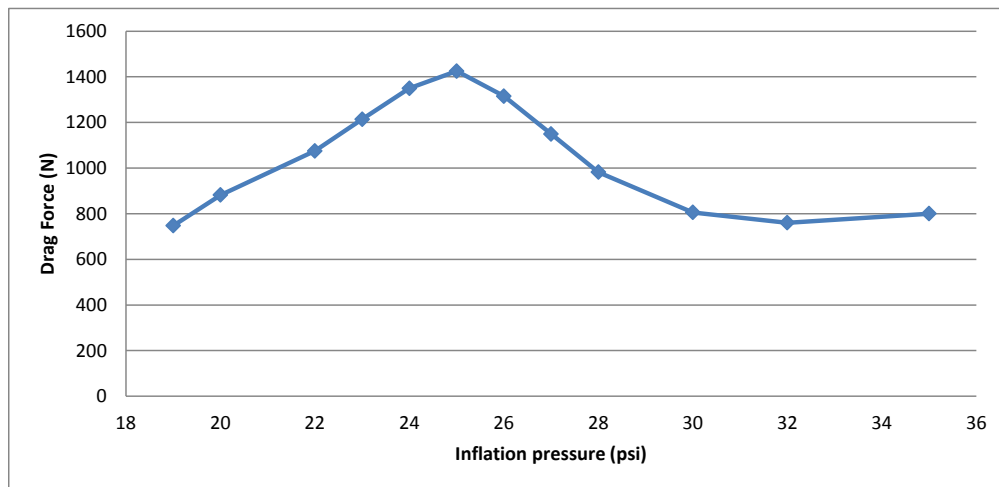- Standing water film thickness – 1 mm

Figure 3.16: Effect of inflation pressure to drag force

Based on Figure 3.16, drag forced has the highest value when the inflation pressure is 25 psi. When the inflation pressure is lower than its standard value, the tire carcass becomes more flexible and falters under the tire load. Therefore, tire load is mostly transferred to the ground through the side walls of tire. This leads to a low pressure distribution in the middle of the contact patch which could cause the reduction in the drag force build-up. However, when the inflation pressure is higher than its standard value, the tire carcass becomes stiffer and decreases the contact patch area leading to a decrease in drag force. Therefore, it can be concluded that when the tire operates at the inflation pressure closer to its standard value, the drag forces are high as seen in Figure 3.17.

3.6.4 Effect of tire contact width on drag force

The tire contact width was varied from 80 mm to 105 mm while keeping the following parameters constant at the indicated values;

- Sliding speed – 45 mph

- Tire inflation pressure – 25 psi

- Average roughness height – 0.1 mm

- Tire load – 4850 N

- Standing water film thickness – 1 mm

The results are plotted in Figure 3.17. Based on that, the drag force decreases with increasing tire width until 100 mm and then increases when the tire width is increased further. It must be noted that there are two opposing factors affecting the drag force in this situation. First is the water film thickness which increases with increasing tire width and causes the decrease in the drag force. This is the reason for observing an initial

decreasing trend in the drag force. The second other factor is the contact area which increases with increasing tire width and causes the increase in drag force. When combining both increasing and decreasing trends of drag forces with tire width, initially the drag force will decrease up to a certain value and then increases.

Figure 3.17: Effect of tire contact width to drag force
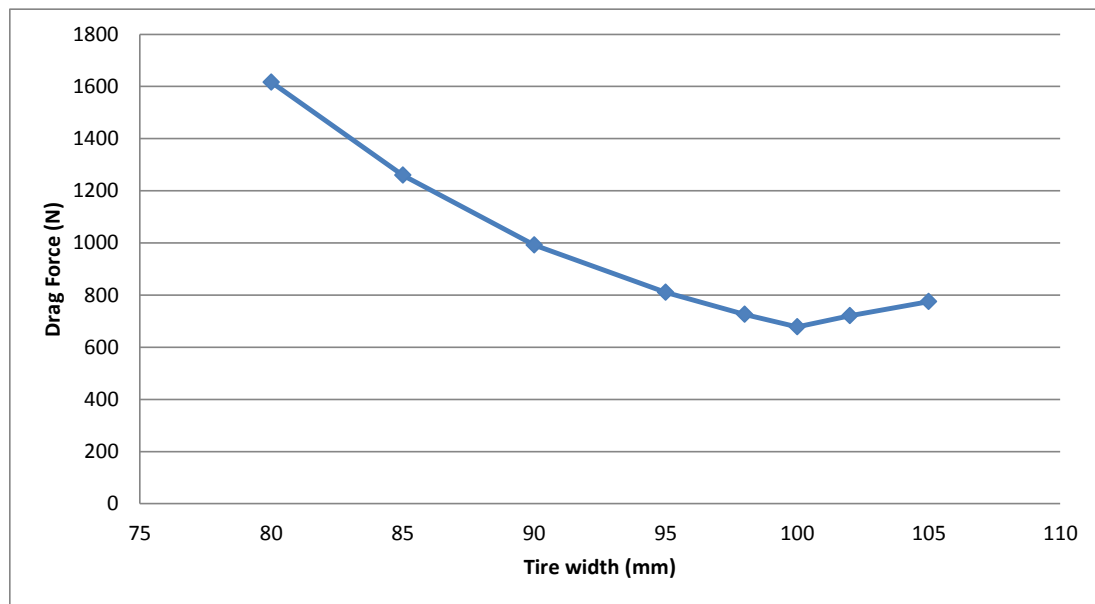
3.6.5 Effect of average roughness height to drag force

The average roughness height was varied from 0.1 mm to 3 mm while keeping the following parameters constant at the indicated values and the results are plotted in Figure 3.18;

- Sliding speed – 45 mph

- Tire inflation pressure – 25 psi

- Tire width – 80 mm

- Tire load – 4850 N

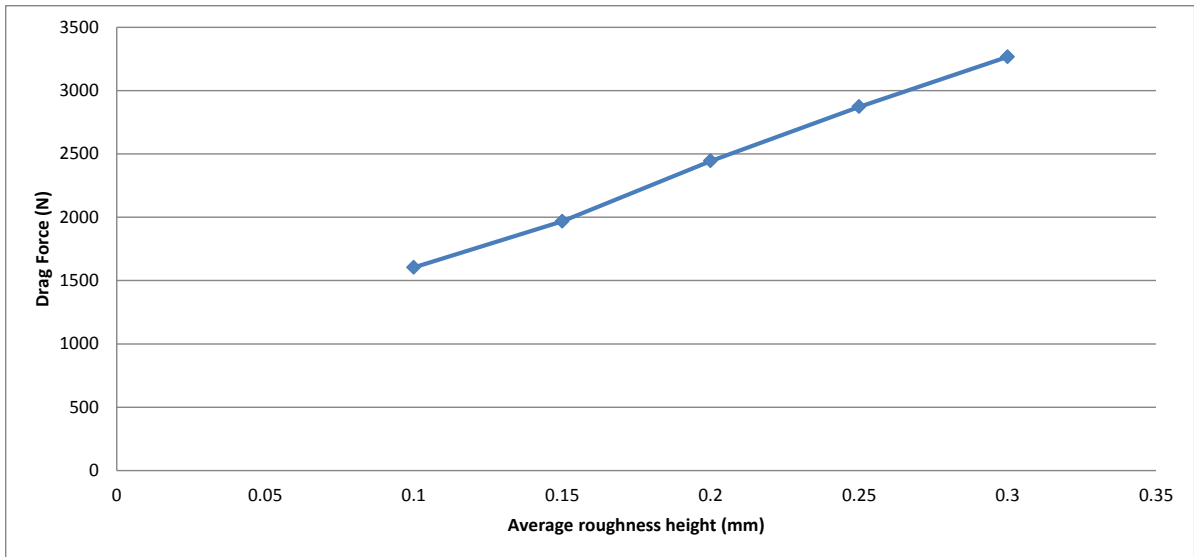- Standing water film thickness – 1 mm

Figure 3.18: Effect of average roughness height to drag force

Based on Figure 3.18 the drag force increases with increasing tire width. This could be due to the fact that increasing roughness height decreases the average film thickness thereby increasing the drag force.

3.7 Comparison with field experiments

Locked wheel skid tests were performed at a selected site on a wet pavement with an average standing water film thickness of 6.5 mm at four different speeds (30 mph, 40 mph, 50 mph, 60 mph). Then the field texture measurements were observed on the test wheel path using a CT meter. The average texture depth (MTD) was calculated and used as an input to the MATLAB program that generates a randomly rough pavement for the above pavement site, the MTD value was 1.12 mm. The program was then assigned the same standing water film thickness and the analysis was performed for different speeds while calculating drag forces. Figure 3.19 shows the two plots of experimental and numerical results. Based on the plot, the numerical model under predicts the results. This could be because the numerical model is only capable of simulating laminar conditions

between the tire and the pavement whereas in reality the flow conditions are turbulent on rough pavements.

3.8 Analysis of the limitations or assumptions of the model

This model has a simple 3D tire with radial springs which is capable of simulating linear material properties. However the real Locked wheel tire has both geometric and material nonlinear characteristics with the structure of the tire being a shell. Also the water flow in the simulation assumes simple laminar flow characteristics. However in the real situation the water flow between the tire and the pavement is more complicated and has laminar, turbulent and flow separation effects. Therefore the real water flow is more complicated than the water flow in the model. After considering all the above facts, it would be difficult to compare the model predictions and the results of corresponding field experiments.
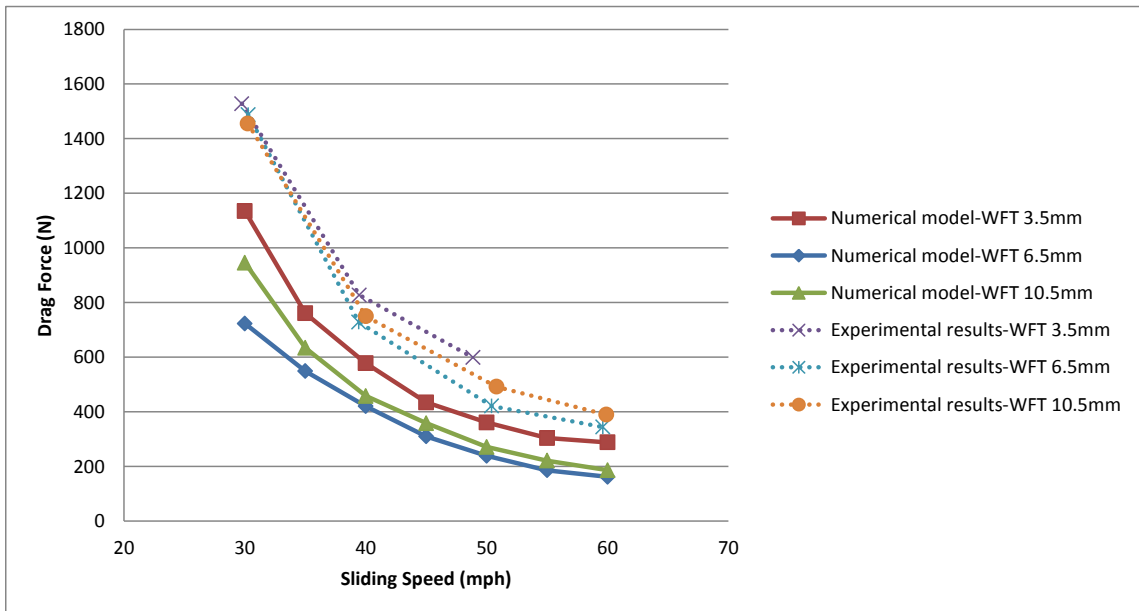

Figure 3.19: Comparison of numerical model and field experiments

3.9 Conclusions

The numerical model predicts drag forces on a tire sliding on a wet random rough surface. A parametric study based on the model predictions is agreeable with the physical principles. This model has a simple 3D tire with radial springs which is capable of simulating linear material properties. However the real Locked wheel tire has both geometric and material nonlinear characteristics with the structure of the tire being a shell. Also the water flow in the simulation assumes simple laminar flow characteristics. However in the real situation the water flow between the tire and the pavement is more complicated and has laminar, turbulent and flow separation effects. Therefore the real water flow is more complicated than the water flow in the model. After considering all the above facts, it would be difficult to compare the model predictions and the results of corresponding field experiments.

CHAPTER 4

CONCLUSIONS AND RECOMMENDATIONS

4.1 Summary of conclusions

The author contributed to the state of the art by simulating a randomly rough pavement in the moist pavement friction model and wet the drag friction simulation model. In the moist friction model, the potential use of a finite element (FE) model and an analytical model that have the capability of predicting friction on a moist pavement based on pavement and tire properties were investigated. Predictions of both models on a selected asphalt concrete test surface matched reasonably well with each other although they exhibited opposite trends with increasing speed. The friction models considered in the moist friction study can be used to simulate any desired field condition. It can also be used to verify a selected number of critical friction conditions when field testing capabilities are limited.

The wet friction model can predict drag forces on a tire sliding on a wet randomly rough surface. A parametric study that was performed based on the model predictions produces results that are intuitive and agreeable with physical principles. The numerical model considered in wet friction study can be used to model the traction force on a tire sliding on a wet pavement.

4.2 Recommendation for further research

This research has identified some areas that can be pursued for further research to gain a better understanding of tire friction or wet traction modeling. One major limitation of the modeling is the assignment of approximate material properties. Therefore further work is needed to evaluate appropriate material parameters for a locked wheel tire. The tire model in the wet friction or drag force simulation is developed based on the assumption of elastic behavior of the tire. Therefore further work is needed to develop techniques to model nonlinear the actual nonlinear tire properties. This research focuses primarily on modeling moist or wet friction acting on a smooth locked wheel skid tester tire. In the future it could be extended to all types of sliding or rolling tires even with treads on them.

REFERENCES

1. Wriggers, P. Reinelt, J. Multi-scale approach for frictional contact of elastomers on rough rigid surfaces, Computer Methods Appl. Mech. Eng. 198 (2009).

2. International Organization for Standardization (ISO). "Characterization of pavement texture by use of surface profiles Part 1: Determination of mean profile depth (1997)," International Standard No. 12.5472.5-1.

3. Hydrodynamics of tire hydroplaning, NASA contractor report, Georgia Institute of Technology, Atlanta, GA. (1966).

4. ASTM Standard E 1960-07 Standard Practice for Calculating International Friction Index of a Pavement Surface, ASTM International, (2007) West Conshohocken, PA.

5. ASTM Standard E 1845-01Standard Practice for Calculating Pavement Macrotexture Mean Profile Depth, , ASTM International, (2001) West Conshohocken, PA.

6. ASTM Standard E 274-06 Standard Test Method for Skid Resistance of Paved Surfaces Using a Full-Scale Tire, ASTM International (2006), West Conshohocken, PA.

7. Benedetto, A., "A decision support system for the safety of airport runways: the case of heavy rainstorms", Transportation Research Part A, 2.56 (2002), 665-682.

8. Dahl, P. A Solid Friction Model. TOR-0158H2.5107–18I-1. California: The Aerospace Corporation (1968).

9. Fwa, T.F., and Ong, G.P., "Wet-pavement hydroplaning risk and skid-resistance: Analysis", ASCE Journal of Transportation Engineering, Vol. 12.54, No. 5, May (2008).

10. Cho, J.R., Lee, H.W., Sohn, J.S., Kim G.J., and Woo, J.S., "Numerical Investigation of the hydroplaning characteristics of three-dimensional patterned tire", European Journal of Mechanics A/Solids, 25 (2006).

11. Ong, G.P. and Fwa, T.F., "Wet-pavement hydroplaning risk and skid-resistance: Modeling", ASCE Journal of Transportation Engineering, Vol. 12.52.5, No. 10, October (2007).

12. Kummer, H. W., and W. E. Meyer, Tentative Skid-Resistance Requirements for main Rural Highways, NCHRP -2.57, Highway Research Board, National Research Council, (1967).

13. Moore, D., "The friction of pneumatic tires", Elsevier Scientific Publishing Co., New York, (1975).

14. Ranganathan, Preventing wet runway accidents. The Hindu, (2005).

15. Risks and factors affected with operations on runways affected by snow, slush, or water, National Air Traffic Services Ltd, (2006).

16. Civil Aviation Report, CAA, (2008).

17. Armstrong-H,. A survey of models, analysis tools and compensation methods for the control of machines with friction. Automatica, 2.50(7), pp. 1082.5-112.58. (1994).

18. Schallamach A., Proceedings of the Royal Society of London, B66, pg. 2.586-2.592, (1952).

19. Schallamach A., "A Theory of Dynamic Rubber Friction," Wear, Vol. 6, No. 5, pg. 2.575-2.582, (1963).

20. Leu M. C., and J. J. Henry, "Prediction of Skid Resistance as a function of Speed from Pavement Texture," TRR 946, Transportation Research Board, National Research Council, Washington D.C., (1983).

21. Rado Z. Analysis of Texture Profiles, PTI Report 9510, Pennsylvania Transportation Institute, State College Park, Pa., (1994).

22. ANSYS 12.0 Software manual, ASSYS Inco. (2004).

23. NCHRP web document 16.

24. Venner, C.H., Lubrech, T., Multilevel methods in lubrication, Tribology Series 37. Elsevier, (2005).

25. Horne, W. B., Joyner, U. T., "Pneumatic tire hydroplaning and some effects on vehicle performance", SAE paper 97, (1965).

26. Chae, S., El-Gindy, M., Johansson, I., Oijer, F., Trivedi, M. "In-Plane and Out-of-Plane Dynamic Response Predictions of a Truck Tire Using Detailed Finite Element and Rigid Ring Models" ASME International Mechanical Engineering Congress and Exposition, Florida, USA, (2005).

27. Lorenz B., Contact Mechanics and Friction of Elastic Solids on Hard and Rough Substrates, (2012).

28. Integrated Tyre and Road Interaction, Development of a Tire – Road Friction Model, Institute for Road and Traffic Engineering, Technical University of Aachen, (2006).

29. Johnson, K.L. Adhesion and friction between a smooth elastic spherical asperity and a plane surface, Cambridge University, 1 New Square, Cambridge CB1 1EY, UK, (1997).

30. American Concrete Pavement Association. Slab Stabilization Guidelines for Concrete Pavements. Technical Bulletin TB018P. ACPA, Skokie, IL. (1994).